POLITECNICO
MILANO 1863

SCUOLA DI INGEGNERIA INDUSTRIALE
E DELL'INFORMAZIONE

Studying local orders in $YBa_2Cu_3O_{7-\delta}$ by nanoscale confinement

Tesi di Laurea Magistrale in
Physics Engineering - Ingegneria Fisica

Author: **Andrea D'Alessio**

Student ID: 945018
Advisor: Prof. Giacomo Ghiringhelli
Co-advisors: Dr. Riccardo Arpaia and Prof. Floriana Lombardi
Academic Year: 2021-22

Abstract

In 1986 scientists were amazed by the discovery of materials that conducted electricity without any resistance at temperatures much higher than previously thought, an accomplishment awarded the Nobel Prize in Physics already the following year. This led to great excitement and the hope one would be able to design materials that would be 'superconducting', as the phenomenon is called, even at room temperature, the holy grail of superconductivity research. The possibility to dispense the use of expensive and cumbersome cooling would indeed revolutionize many technologies like electrified transports, and also lay the foundation for the next generation of green innovations. However, despite intense research, many open questions remain and the mechanism behind high temperature superconductivity still represent a puzzle, far from being fully understood. Recently, the most common idea is that the comprehension of the superconducting mechanism cannot prescind from the understanding of the normal state of these materials. This is also unconventional, and populated by a constellation of local orders, characterized by nanoscale lengths: here, charge, spin, lattice and orbitals have a role, but their entwining and mutual relations are still not fully understood. The core of cuprate high-T_c superconductors (HTS) is represented by the CuO_2 planes, where superconductivity sets in and where all the symmetry breaking orders reside. In order to succeed in understanding these fascinating materials, an innovative strategy is to confine the CuO_2 planes at the nanoscale in HTS, and to use strain and confinement as a knob to tune the orders both in the superconducting and in the normal state. This can be done only if HTS are shrunk in thin film form, preserving the bulk quality. In this way, confining the orders on the same scale of their characteristic lengths, one may expect the locality of charge, spin and current orders to be enhanced, possibly simplifying the physics at play. The confinement can be obtained in two ways, either by nanopatterning c-axis oriented HTS thin film, where the CuO_2 planes take the shape of the nanostructures, or depositing a-axis oriented HTS nm-thin films, where the CuO_2 planes form nanoribbons, constrained on either side by vacuum and the underlying substrate. In this thesis work we have followed both of these strategies, using c-axis and a-axis oriented $YBa_2Cu_3O_{7-\delta}$ thin films.

Keywords: High Temperature Superconductors, YBCO, Nanoscale orderings, Nematic-

ity

Abstract in lingua italiana

Nel 1986 scienziati di tutto il mondo rimasero impressionati dalla scoperta di un materiale in grado di condurre elettricità senza alcun tipo di resistenza a temperature molto più alte di quanto si ritenesse prima possibile, un traguardo che valse il premio Nobel per la fisica già l'anno successivo. Questo portò un gran fermento e la speranza che un giorno si sarebbe stati in grado di produrre materiali 'superconduttivi', come viene definito il fenomeno, anche a temperatura ambiente, il sacro Graal della ricerca sulla superconduttività. La possibilità di fare a meno di costosi e ingombranti sistemi di raffreddamento rivoluzionerebbe infatti molteplici tecnologie come i trasporti a elettricità, e porrebbe le fondamnenta per la futura generazione di tecnologie verdi. Ad ogni modo, nonostante intensa ricerca, rimangono aperti molti interrogativi e il meccanismo che si cela dietro la superconduttività ad alta temperatura critica rimane ancora un puzzle, lontano dall'essere pienamente compreso. Recentemente, l'idea più diffusa è che la comprensione del meccanismo della superconduttività non può prescindere dalla comprensione dello stato normale di questi materiali. Anch'esso è infatti non convenzionale, popolato da una costellazione di ordini locali, caratterizzati da una lunghezza nanometrica: qui entrano in gioco spin, reticolo cristallino e orbitali atomici, ma il discernimento di ogni singolo ruolo e la loro mutua interazione non sono ancora pienamente compresi. Il nucleo dei superconduttori cuprati ad alta temperatura critica è rappresentato dai piani di CuO_2, dove si stabilisce la superconduttività e dove risiedono tutti gli ordini che rompono la simmetria del materiale. Al fine di riuscire a comprendere questi affascinanti materiali, una possibile strategia da mettere in atto è quella di confinare i piani di CuO_2 alla nanoscala, e usare lo strain e il confinamento come fossero una manopola per regolare gli ordini sia nello stato superconduttivo che in quello normale. Ciò è possibile solamente se si riesce a comprimere gli HTS (High Temperature Superconductors, Superconduttori ad alta temperatura critica) nella forma di film sottile, conservando le proprietà del bulk. In questa maniera, confinando gli ordini alla stessa scala della loro lunghezza caratteristica, ci si può aspettare che le località degli ordini di corrente, carica e spin siano amplificate, semplificando se possibile la fisica in gioco. Il confinamento può essere ottenuto in due modi, sia attraverso il nanopatterning di film di HTS orientati lungo l'asse c, dove i piani di CuO_2 prendono

la forma di nanostrutture, sia depositando film di HTS orientati lungo l'asse a, dove i piani di CuO_2 formano dei 'nanoribbon' delimitati da un lato dal substrato e dall'altro dal vuoto. In questo lavoro di tesi abbiamo seguito entrambe le strategie, servendoci di film di $YBa_2Cu_3O_{7-\delta}$ orientati sia lungo l'asse a che lungo l'asse c.

Parole chiave: Superconduttori ad alta temperatura critica, YBCO, Ordini alla nanoscala, Nematicità

Contents

Introduction

The understanding of high temperature superconductivity in cuprates, whose discovery dates back to 1986, remains one of the greatest challenges of condensed matter physics. Within this class of compounds, the highest superconducting critical temperature T_c has been measured in HgBaCaCuO, where its value is 135 K at atmospheric pressure and even higher when high pressures are applied. Cuprates are a class of materials whose remarkable superconducting properties have attracted the interest of the solid state physics community for more than three decades. These complex copper oxides show transition temperatures which are higher than the limit predicted by BCS theory, the main theory allowing to explain superconductivity at a microscopic level. The microscopic mechanism responsible of superconductivity in cuprates still remains a mystery and it is believed that its understanding could open the door to the the engineering of new materials with even higher T_c. The comprehension of the normal state is considered the key to unravel the secrets of HTS, but also there the picture is very unconventional, with properties which challenge the concept of Fermi-Landau quasiparticles, on which ordinary metals are based.

The study of cuprates is therefore one of the main research areas in condensed matter physics, but the complexity of their behavior makes it an extremely difficult task. By varying the temperature or altering their chemical composition we observe a multitude of orders and excitations, both in the normal and in the superconducting state, among which we cannot simply establish a mere competition, but more of an intricate inter-dependence: the scientific community is therefore still unable to find a valid and universally accepted theoretical model to describe the full picture. The experimental activity is therefore invested of a central role in this complicated process, having to provide new elements to shed some light on this intricate intertwining of orders. A conventional approach is no longer sufficient and new experiments have to be designed, in order to modify or enhance these orderings, or even create "new materials" in which constraints can make their reciprocal relations to stand out.

The novel strategy on which this thesis work is based is to study HTS confined at the nanoscale. The main lengths that define cuprate HTS (the coherence length ξ, the London penetration depth λ and the charge and spin modulations correlation lengths) are on the

order of the nanometers and fabricating nanostructures whose dimensions are comparable to these length scales could potentially provide a great contribution to the study of HTS. Shrinking down HTS at the nanoscale implies the confinement of the CuO_2 planes, which are the core elements in the structure of HTS, since both superconductivity and the main symmetry breaking orders populating the phase diagram reside there.

To confine CuO_2 planes we have followed two different approaches. The first one is to pattern nanowires on *c*-axis oriented YBCO thin films. These nanowires have been instrumental to the investigation of the nematic order in the superconducting state. This order breaks the four-fold symmetry of the HTS lattice, and profoundly modifies the transport properties of HTS. Its evidence is still very elusive, although confirmed by several experimental techniques, in the normal state, while it has never been observed in the superconducting state. Measuring the critical current density J_c in nanowires patterned at different in-plane angles, we have the possibility to check if an unexpected anisotropy in J_c is present, which should be connected to the presence of a nematic superconducting condensate. The second approach is based on the realization of *a*-axis oriented YBCO thin films, spanning the whole underdoped region of the phase diagram. Here, the CuO_2 planes are confined by the thickness of the film and form nanoribbons, all arranged in series perpendicularly to the substrate. This peculiar approach can allow us to investigate YBCO transport properties from a different perspective, possibly modifying the coupling between adjacent planes, along the *c*-axis direction, and influencing the different orders, i.e. the charge order, populating the underdoped side of the phase diagram.

The outline of the thesis is the following:

In chapter 1 a small overview of superconductivity is provided, highlighting historical milestones and some fundamental theories. We introduce High Temperature Superconductors (HTS) and we talk about cuprate superconductors, in particular YBCO, the material object of this thesis work.

In chapter 2 we will discuss about the deposition of YBCO thin films and their morphological, structural and electrical characterization.

In chapter 3 we write about the nanofabrication procedure, used to pattern *c*-axis oriented YBCO thin films.

In chapters 4 and 5 we present and discuss the experimental results. In particular, in the former chapter we focus on the study of nematicity in *c*-axis YBCO nanowires and in the latter we present the results of the measurements carried out on the *a*-axis oriented films.

Finally, in the last chapter we briefly summarized the main achievements of the thesis,

and discuss about the possible outlooks.

1 | Background

In this chapter we will provide a brief summary of the history of superconductivity. Some of the theory which describes the behavior of superconductors will be highlighted, in order to provide a background useful for the understanding of the thesis work.

1.1. Brief historical overview of superconductivity

- 1911. While conducting experiments with liquid helium, Kamerlingh Onnes discovers that going below a certain temperature the resistance of mercury rapidly vanishes. Perfect conductivity below a critical temperature, T_c, becomes the first hallmark of this new class of materials, which will be called superconductors.
- 1933. Walther Meissner and Robert Ochsenfeld observe that superconductors are characterized by a perfect diamagnetism. A magnetic field less than a critical value, B_c, is excluded from the bulk of a superconductor when the latter is cooled down below T_c (the so-called Meissner effect) [1]. This is the second and perhaps most significant signature of superconductivity, which contributes to isolate superconductors from others materials and elevate their behavior to peculiar and worth of thorough study.
- 1935. Fritz and Heinz London develop two equations, which are able to account for the two main characteristics of superconductors mentioned above [2]. These two fundamental equations relate the electromagnetic field to current in superconductors, and their expression is the following:

$$\partial_t \boldsymbol{J_s} = \frac{n_s e^{*2}}{m^*} \boldsymbol{E} \tag{1.1}$$

$$\nabla \times \boldsymbol{J_s} = \frac{n_s e^{*2}}{m^*} \boldsymbol{B} \tag{1.2}$$

where $\boldsymbol{J_s}$ is the superconducting current density, $\boldsymbol{E}$ and $\boldsymbol{B}$ are respectively the electric and magnetic field inside the superconductor, n_s is the density of super-

conducting carriers which flow without dissipation, m^* and e^* are respectively the effective mass and the effective charge of superconducting electrons (which are generally assumed to take double the value of the mass and the elementary charge in the normal state, which would be the rest mass and the charge of the electron). The equation 1.1 describes the perfect conductivity, while the other, combined with the Ampere's law, takes care of explaining the Meissner effect:

$$\nabla^2 \boldsymbol{B} = \frac{1}{\lambda_L^2}\boldsymbol{B}, \qquad \lambda_L \equiv \sqrt{\frac{m^*}{\mu_0 n_s e^{*2}}} \tag{1.3}$$

with μ_0 corresponding to the vacuum magnetic permeability. When we enter the bulk of the material, we have that there is a complete screening of the magnetic field due to the formation of screening currents flowing in a thin region at the surface of the superconductor. Both the screening currents and the magnetic field decay exponentially into the superconductor from its surface with a characteristic length given by λ_L, which is known as London penetration depth.

- 1950. Ginzburg and Landau postulate a phenomenological model [3], based mainly on thermodynamical considerations; this model picked up on Landau's previously established theory regarding second-order phase transitions and extended it, incorporating London's theory into the picture by considering the superfluid density $n_s(\boldsymbol{r})$ as a function of spatial variables. A complex wavefunction, related to the superfluid density, is introduced, and is defined as:

$$\Psi(\boldsymbol{r}) = |\Psi(\boldsymbol{r})| e^{i\phi(\boldsymbol{r})} \tag{1.4}$$

where $|\Psi(\boldsymbol{r})| = \sqrt{n_s(\boldsymbol{r})}$ is the amplitude and $\phi(\boldsymbol{r})$ is the phase as a function of the position. The theory is postulated close to the superconducting temperature, where the order parameter is assumed to be small and slowly varying. One can then expand in series the expression of the free energy of the system, immersed in a magnetic field $\boldsymbol{B}$. The equilibrium wavefunction can be found minimizing the expression of the free energy. From the final expression can be extracted a second characteristic length, representing the distance at which the order parameter can vary and not cause a significant energy increase of the system. Its expression is the following:

$$\xi \equiv \sqrt{\frac{\hbar^2}{2m^*|\alpha|}} \tag{1.5}$$

- 1950. Maxwell observes the isotope effect for Hg, discovering that the T_c is inversely proportional to the root of the mass of the isotope of which the material it's made [4]. Since the phonon frequency shows the same kind of dependence with respect to the lattice atoms oscillating mass, this discovery would point directly to a possible relation between the electron-phonon coupling and the superconducting phenomenon.
- 1957. Bardeen, Cooper and Schrieffer come up with the first microscopic theory of superconductivity [5], providing a successful framework within which to understand and describe conventional superconductors. The fundamental insight of BCS theory is that electrons, which would normally be subject to Coulomb repulsion, form pairs through the mediation of a phonon and condense into a phase that could be assimilated to a superfluid state. If the energy of the phonon is too high, the electrons cannot couple through lattice vibrations in a sustainable way, reason for which 30 K was believed to be the upper limit for the critical temperature of superconductors.
- In 1986 Bednorz and Müller discovered a new class of materials with a T_c roughly equal to 35 K, greater than one predicted by BCS, and this can definitely be marked as one of the major scientific breakthroughs of the last decades. The first material to show this remarkably high T_c was BaLaCuO; few months later another cuprate, $YBa_2Cu_3O_{7-\delta}$, was discovered, with a record T_c of 92 K, higher than the boiling point of nitrogen.

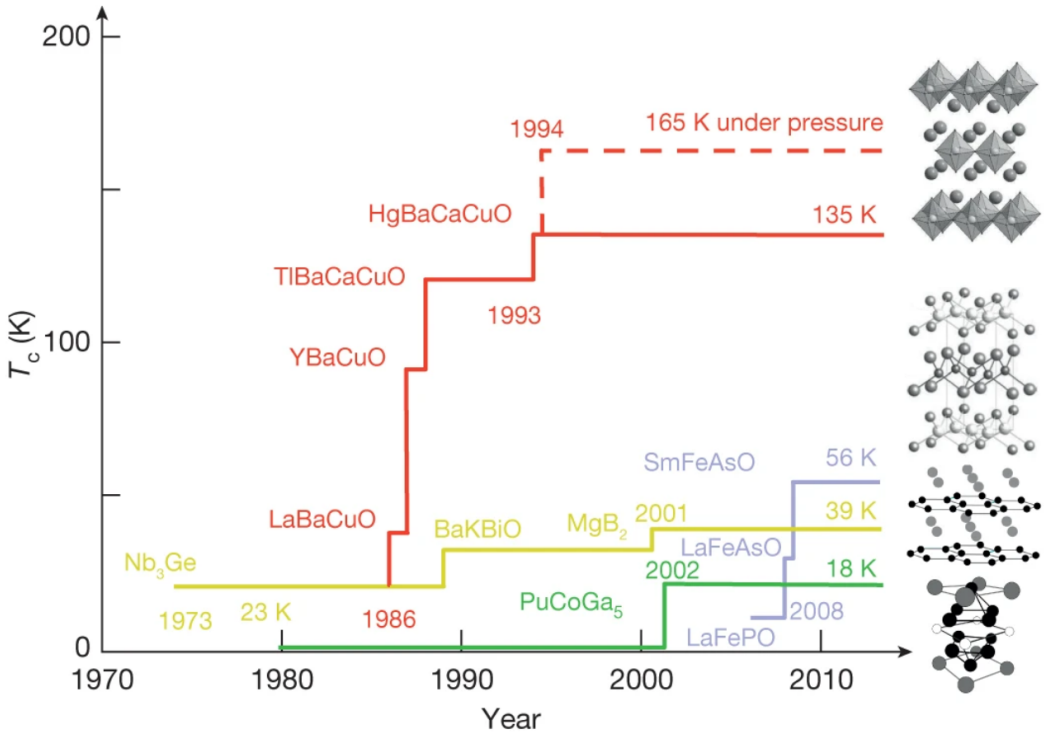

Figure 1.1: In this graph [6], we can see the superconducting transition temperature of a given superconductor versus the year of its discovery. On the right we can find the respective crystal structure. Every colour corresponds to a family of superconducting materials, with the cuprates (in red) being the one with the highest T_c. In light purple we have a class of materials which has attracted much interest in the last years, the iron-based superconductors.

1.2. High-T_c superconductors and YBCO

Other cuprate HTS have been discovered since then (see fig. 1.1), with even higher critical temperature, but after more than 30 years from their discovery a unified and universally accepted theory to explain this 'unconventional' behavior has not been found.

In this thesis work we will focus on YBCO. The $YBa_2Cu_3O_6$ unit cell (see fig. 1.2) consists of three perovskite cells on top of each other. Each perovskite unit cell contains a Y or Ba atom at the center: Ba in the bottom and in the top unit cells, Y in the middle one. Cu atoms occupy all the corner sites, while oxygens are placed in the middle edge positions. The CuO_2 planes are located right above and below the Y ion. The chemistry of YBCO amplifies the Coulomb repulsion between electrons. Looking at its structure we can identify two-dimensional copper oxide layers, separated by ionic, electronically inert, buffer layers.

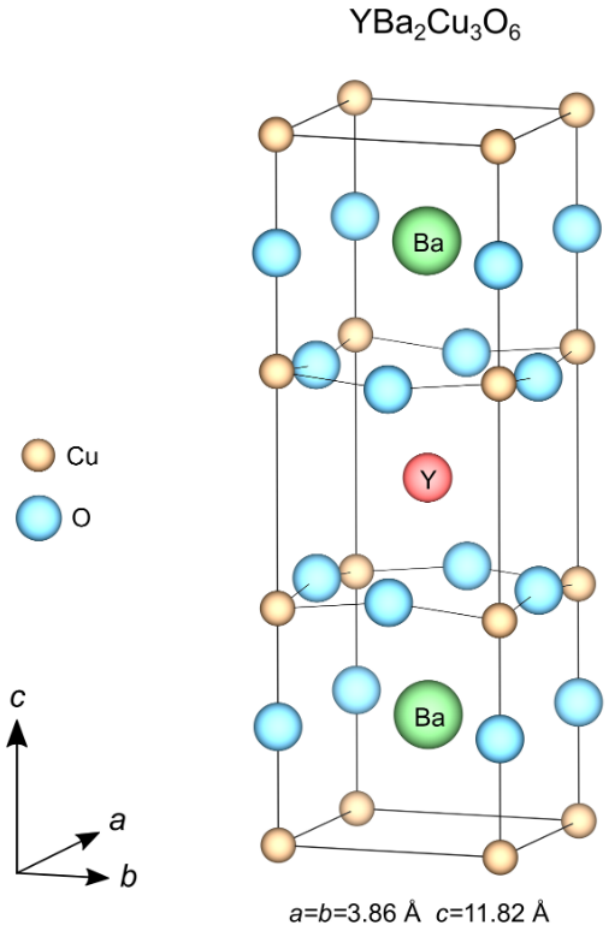

Figure 1.2: Here we have the $YBa_2Cu_3O_6$ unit cell [7], made of three perovskite cells stacked on top of each other; the Yttrium atom is located in the central perovskite cell, while the Barium is on the top-most and bottom-most cells. The three cells are separated by the electronically active CuO_2 planes.

As would happen in the case of well-separated atoms, the electronic orbitals that describe the states formed in the CuO_2 planes are well localized, and it takes a large amount of energy to transfer an electron from one site to another. This produces what can be called a "traffic jam of electrons", resulting in poor conductivity (Mott insulator). At room temperature is such a bad conductor that, according to the theory of conventional superconductors, YBCO and, more generally, copper oxides, would have seemed the least likely materials where to look for superconductivity. The CuO_2 planes can be 'doped' by altering the chemical makeup of what we referred to as buffer layers, which act as a sort of charge reservoir. We can either add electrons (electron doping) or remove them (hole doping), influencing the physical properties of the system. For the purposes of this work, our discussion will be limited to hole-doped systems, and in particular to YBCO.

In YBCO, the doping consists in adding oxygens at the top and bottom planes of the unit cell, which will arrange themselves exclusively along the [010] direction, giving rise to the oxygen chains. The presence of the oxygen facilitates the motion of electrons along that direction, which would otherwise be hindered by the Pauli exclusion principle, making the b-axis more conductive than the a-axis.

The cuprate high-T_c superconductors are all layered compounds where the CuO_2 planes steer all the electronic properties that characterize them. Those planes are only weakly coupled between each other, reason for which the out-of-plane properties differ a lot from the in-plane ones. Cuprates are superconductors of type II, defined by a region in which they still exhibit superconducting behaviour even tough they allow the penetration of magnetic field through the material. They are not conventional superconductors, that is their properties cannot be described in terms of BCS theory. In contrast to low-T_c conventional superconductors, in which the superconducting energy gap, and therefore the pairing of electrons into Cooper pairs, are isotropic (can be described by a $s-wave$ order parameter), the gap in cuprates presents a strong anisotropy. Thanks to phase sensitive experiments it has been possible to show that the gap can be generally described by a $d_{x^2-y^2}$ orbital geometry, with a gap which shows its maxima along the Cu-O bonds and nodes along the diagonals (see fig. 1.3).

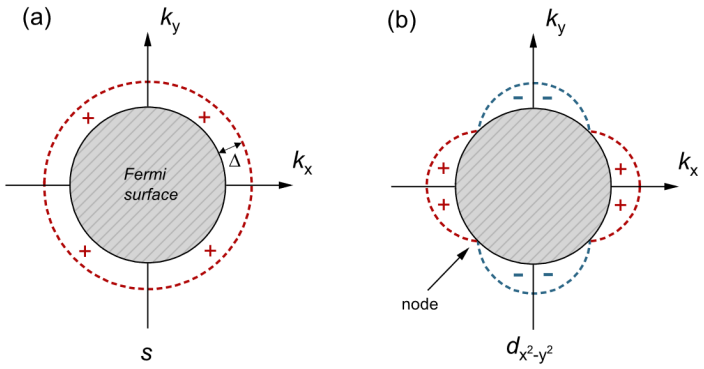

Figure 1.3: This is an illustration of the superconducting energy gap [7] for (a) $s-wave$ order parameter, and for (b), $d-wave$ order parameter on a circular Fermi surface. In the picture is also indicated the sign of the phase of the order parameter, together with the presence of nodes.

1.2.1. The phase diagram

As the study of copper oxides started to be carried out with an ever-increasing level of precision, in the scientific community it was soon realized that the well-understood quantum theories employed to explain the behavior of metals and conventional superconductors were completely inadequate to account for the physical properties of this new class of materials. The main issue appeared to be the high correlation between the electrons, which is capable of giving rise to a plethora of orders and intertwined phases (see picture of the phase diagram, fig. 1.4).

At zero doping every CuO_2 unitary plane has an odd number of electrons, and the spin orientation is still a dynamical degree of freedom. Because of the Pauli exclusion principle, virtual hopping of electrons produces an antiferromagnetic interaction between neighbouring spins, which is responsible for a Neél ordered phase below room temperature; we therefore have static magnetic moments on the Cu sites with an orientation that reverses itself from one Cu to the next.

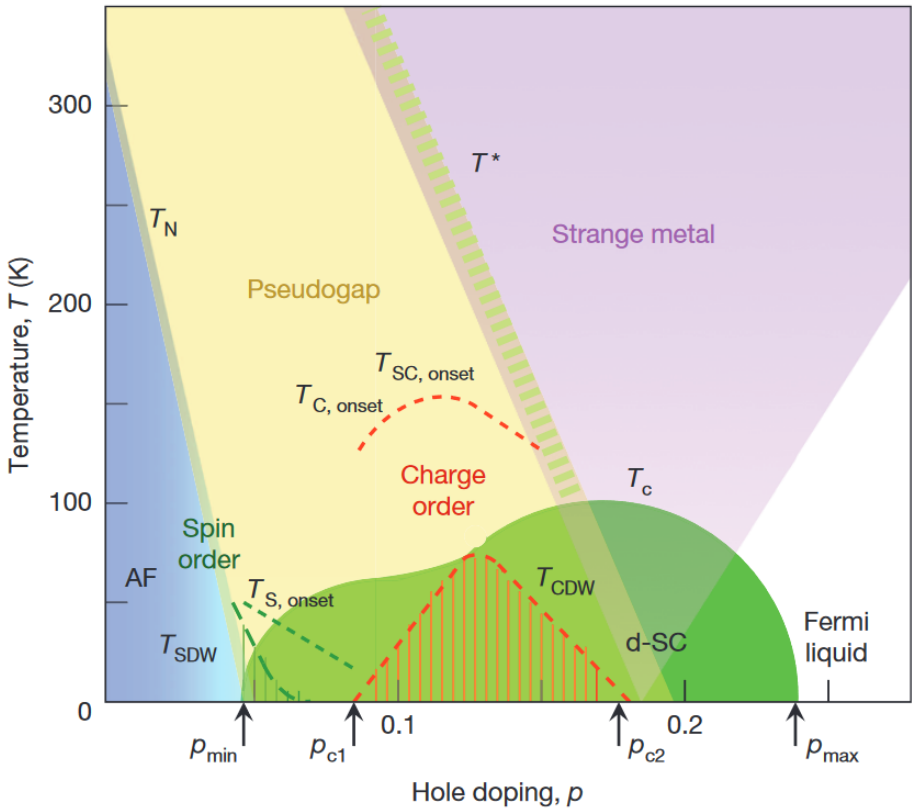

Figure 1.4: Here we have a schematic represantation of the phase diagram of YBCO [6]. As we can see, it is characterized by a multitude of orders, which make the understanding of cuprates superconductivity especially hard. The nematic order has been placed mainly in the underdoped region, even tough its collocation is still object of the scientific debate. It is highlighted the presence of two quantum critical points at two differrent critical dopings, p_{c1} and p_{c2}.

Increasing the doping p (number of oxygens per planar copper atom), a superconducting phase sets in, whose transition temperature grows until we reach p_{opt} (around $p = 0.16 - 0.18$), then decreases before completely vanishing at high enough dopings; we define YBCO with $p < p_{opt}$ underdoped and the one with $p > p_{opt}$ overdoped.

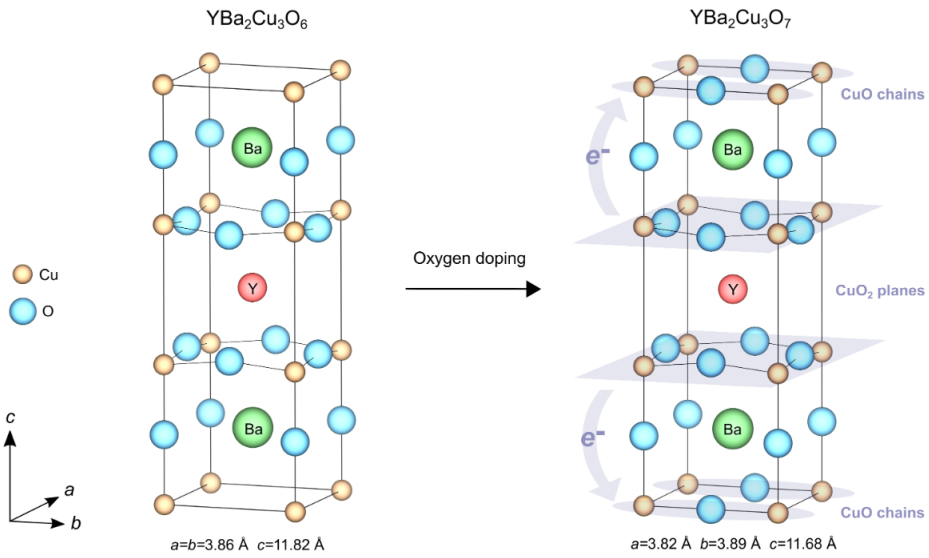

Figure 1.5: Here [7] we have a clear visualization of the doping mechanism: if we add highly electronegative oxygens along the [010] direction of the top-most and bottom-most layers, it attracts electrons from the CuO_2 planes, doping them with holes.

At temperatures well above T_c the resistivity in YBCO is almost two orders of magnitude larger than in simple metals and shows a temperature dependence which is linear, in open contrast with conventional theory of metals; for this reason the regime above T_c has been named "bad metal" or, more commonly, "strange metal", and is perhaps recognized as the most mysterious feature of the cuprates phase diagram. The main characteristic of the strange metal phase is the total absence of quasiparticles, meaning that it cannot be described in terms of the Fermi liquid theory; although much of its behavior can be explained in the frame of the so called "marginal Fermi liquid theory", where quasiparticles are spoiled, an unanimous understanding is still missing.

In the underdoped regime, at temperatures just above T_c we observe a unique behavior, peculiar to the copper HTS, which takes the name of pseudogap regime. It is characterized by a considerable suppression of the electronic density of states at lower energies that cannot be simply explained through the occurrence of any form of broken symmetry. The pseudogap regime appears below a temperature T^*, where the linear-in-temperature resistivity typical of the strange metal is spoiled, and the appearance of a partial gap is observed in spectroscopic data. The existence of such regime was first deduced by nuclear magnetic resonance measurements, which revealed a reduction in the low-frequency spin excitations. A mapping of the pseudogap in the k-space was directly carried out with angular resolved photo-emission spectroscopy measurements. The resulting structure was

found to be roughly similar to the $d-wave$ superconducting gap, at least from the symmetry point of view. We can in fact observe the suppression of the density of states only in the antinodal region of the Brillouin zone, where the $d-wave$ gap is the largest. According to some theories, Cooper pairs start to form already at temperatures close to T^*, which are quite higher than the onset of the superconducting state. This could be explained by the presence of quantum phase fluctuations that prevent the settling of superconductivity until much lower temperatures are reached, even though the notion of pairing correlations in absence of a substantial phase coherence is rather far-reaching. Pervading all the underdoped region of the phase diagram, a nematic order is far from being fully understood. Nematicity can be found in liquid crystals and is characterized by the presence of a preferential direction, along which the crystals are aligned. In the case of cuprates, nematic order determines the breaking of full rotational symmetry, still preserving a translational invariance of the physical properties. Moving at low temperature from the antiferromagnetic insulating-like region to the superconducting phase, we can find a further magnetic order, the so-called Spin Density Wave (SPDW), a periodic modulation of the of the electronic spin density [8] [9]. This kind of spin order differentiates itself from the the AF order at really low doping since SDW is incommensurate and uniaxial, along the a-axis. At few K, SDW is static, while it becomes fluctuating at higher temperatures [10] [11]. In the underdoped region there is a last state worth of being mentioned, the Pair Density Wave, which consists in a spatial modulation with finite momentum of the Cooper-pairs density. So far it has been found in two cuprates compounds, LBCO [12] and BSCCO, elevating this order to a generic phase of cuprates [13] and a possible key to explain the pseudogap regime [14].

1.3. Breaking the four-fold rotational symmetry

Among the orders that coexist in the phase diagram, we will focus in the following on two of these, both breaking the four-fold symmetry of the crystal: charge order, of which the main manifestation is the charge density wave (CDW), and the nematic order.

Charge density waves have been successfully probed and widely studied in cuprate HTS in the last ten years. Already in 1950, Rudolph Peierls pointed out that the energy of a metallic one-dimensional chain of atoms would be lowered through a lattice distortion whose wave vector would match the Fermi wave vector. The presence of charge modulating waves was first predicted in cuprates in 1989 [15] [16], trying to study the breakdown of the antiferromagnetic phase upon doping through 3D-fluctuations: these studies indicated a tendency towards the formation of charged magnetic domain lines. In 1995, scientists

found the first evidence of charge ordering in La-based cuprates with a doping of 1/8, in correspondance of which we now know CDWs to be at their strongest [17]. Neutron scattering experiments allowed to find Bragg reflections characteristic of a magnetic superstructure with a periodicity eight times larger than the basic crystallographic unit cell, as well as another set of reflections pointing to a four-unit-cell modulation of the crystal lattice. Being those modulation commensurate, their treatment was limited to the real-space and they were given the name of stripes, since physically one had nanoscale regions with perturbed antiferromagnetic order separated by non-magnetic 'rivers' of charge. This kind of modulation was believed to have both magnetic and electrical nature until 2012, when, by Resonant Inelastic X-ray Scattering (RIXS), pure charge modulations could be observed in the quasi-elastic region of the spectra, i.e. at quasi-zero energy loss [18]. CDW is a biaxial modulation of the density of charge ρ, occurring along the two crystallographic directions a and b in the CuO_2 planes. The q-vector of the modulation is incommensurate with respect to the lattice, meaning that the wavelength of the charge modulation is not an integer multiple of the lattice parameters.

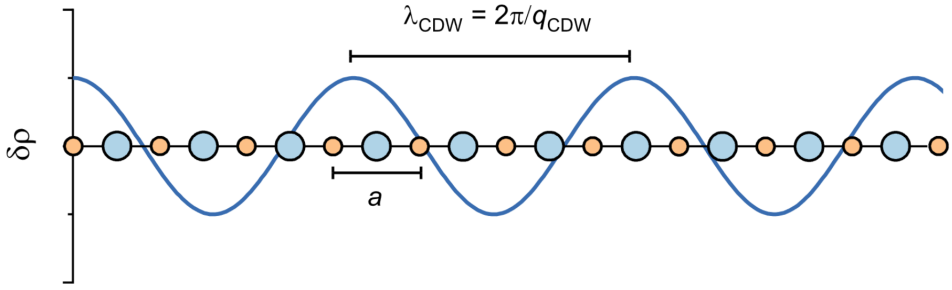

Figure 1.6: This is a 2D representation of the Charge Density Wave (CDW) [7]. We can see a modulation of the density of charge, whose wavelength is incommensurate with respect to the lattice parameter.

This charge ordering is strongly 2D: the correlation length is rather long-ranged, in the order of up to 10 nm along the a and b axis, while along c-axis it is smaller then the distance between adjacent CuO_2 planes [19]. However, a 3D charge density wave has been observed at low temperature and high magnetic field [20] [21]; in contrast to the quasi-2D zero field counterpart the 3D excitation is uniaxial along the b-axis. This experimental evidence is a first signature of entwining/competition between the CDW and the superconducting order.

Evidence of CDW has been found in the underdoped region of the phase diagram, in the doping range $0.08 < p < 0.17$, with an onset temperature which follows a dome-shape

doping dependence having its maximum at $p = 0.12$ [22]. The most notable deviation of the T_c from its parabolic dependence on the doping level happens at $p = 1/8$, where the CDW is the strongest [23]; this feature of the phase diagram points to a close competition between CDW and superconductivity [24] [25], further confirmed by another occurrence. The CDW intensity increases when reducing temperature from the onset temperature down to the critical temperature. When entering the superconducting state, the intensity is instead reduced. However, charge modulations get enhanced below Tc, and upon the application of a magnetic field, which reduces the superconducting pairing [26].

CDW are anisotropic along the the a and b directions of the CuO_2 planes of YBCO, therefore they break the four-fold symmetry of these planes. A large in-plane anisotropy of the values of the Nernst coefficient $\nu(T)$ has been observed in YBCO samples, reaching its maximum at $p = 0.12$, where, as already mentioned, CDW are at their strongest. It is important to stress that CDW are characterized by a spatial modulation of the density of charge and are therefore defined by a finite wave-vector, which allow us to probe them easily with the help of a spectroscopic technique with high resolution. As already said, CDWs have beein found consistently in the underdoped region of the phase diagram and still remains unclear their role in the frame of cuprate superconductors transport behaviour. Recently it has been possible to isolate short-range dynamical charge density fluctuations in addition to the previously known quasi-critical charge density waves. They have been found to persist beyond the pseudogap temperature, pervading a large portion of the cuprates phase diagram [27, 28].

Nematicity, on the other hand, is far more elusive and none of the experimental evidence collected so far can be deemed conclusive in characterizing this still mysterious order. First of all, nematicity is translationally invariant, which makes it really hard to be investigated using spectroscopic techniques, since the elastic scattering component ($\boldsymbol{k}$=0), is always the greatest. The photons probing the nematic order would in fact have zero momentum, like the ones that are elastically scattered (for example by reflections on the surface due to its roughness), and they will be therefore indistinguishable ones from the others in the final energy spectra. Nevertheless, ARPES measurements showed in the pseudogap region some small differences in the circular dichroism [29], whose anisotropy could be associated to the breaking of four-fold rotational symmetry. Among the scientific community there is no unanimous agreement on where to place the nematic order in the phase diagram; resistivity and Nernst coefficient measurements would confine nematicity in the low doping region and in a narrow range of temperatures above Tc, establishing a link with the spin order. O. Cyr-Choiniere *etal.* [30] found two types of nematicity at low doping, one associated to an anisotropy in both transport and Nernst coefficient, and

the other, at slightly higher dopings, reflected in the anisotropy of the sole Nernst coeffiecient, attributed therefore to the short range charge modulations, which are stronger in that region. According to a great part of literature, nematic order would be the symmetry breaking order characterizing the pseudogap, in an attempt to identify this peculiar regime as a self-standing phase of the phase diagram [31]. Transport measurements carried out on LSCO samples point instead to a more diffuse presence of nematicity, whose evidence would not limit itself to the pseudogap but extend to higher doping regions and even at temperatures close to the ambient one (see pic. 1.7). Wu *et al.* [32] patterned on LSCO thin films Hall bars arranged in a sunbeam configuration and performed measurements of the transverse voltage while a probing ('bias') current flows longitudinally; what emerges is a robust and diffuse presence of nematicity, which is indicated by a phase offset of the nematic resistivity modulation influenced by the substrate. Their findings are closely related to previous works where, thanks to different experimental techniques, a breaking of the four-fold rotational symmetry was detected and associated to nematic order; nevertheless, they were able to detect the same anisotropy even in regions of the phase diagram where there is no sign of pseudogap or of superconducting vortices, paving the way to a new understanding of nematicity. Furthermore, the role of the substrate in influencing the character of the anisotropy in the resistivity measurement also points to a crucial role of the strain in influencing nematicity. Measurements that would point to a nematic behaviour have been carried out in other quantum materials, as in magic-angle graphene [33] and kagome lattices [34], indicating the universality of this order and its possible connection to superconductivity.

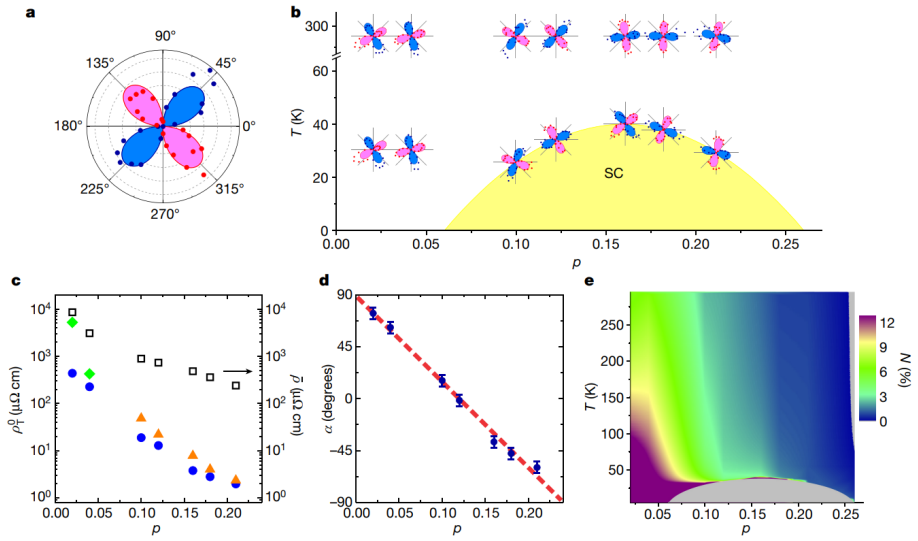

Figure 1.7: This picture [32] shows how a modulation of the resistivity, lead back to a nematic behaviour, could be observed in very diverse regions of the phase diagram, pointing to a nematicity not just limited to the pseudogap.

Despite all this experimental effort, a very strong signature of nematicity has not been yet found in HTS, making this ordering one of the most elusive in the phase diagram. Various scientific works have showed the presence of a two-fold symmetry anisotropy in the measurements of a well-defined physical quantity, but it has never been possible to directly and conclusively tie such anisotropy to a nematic behaviour. The origin of a zero-momentum breaking of the rotational symmetry is rather uncertain and it has been proposed that it could be due to quantum criticality. A quantum critical point is a point of the phase diagram in which a continuous phase transition takes place at 0 K. As in the case of second order phase transitions, going from a disordered to an ordered (characterized by a loss of symmetry) phase is accompanied by fluctuations; in the case of a QCP we have fluctuations of quantum mechanical nature, scale invariant in space and time, and their impact is not limited to a narrow region of the phase diagram, but is felt over a wide range of temperature above the QCP. Antiferromagnetic fluctuations are believed to be one of the main candidates to explain unconventional superconductivity in strongly correlated electron systems like cuprates; in these materials, we have in fact the appearence of a dome-shaped superconducting phase in the vicinity of end point of the antiferromagnetic (AFM) order, where spin fluctuations (SDW) are at their strongest. Nevertheless, scientists are collecting more and more evidence of the presence of unidirectional (nematic) electronic correlations, whose fluctuations could play a key role in superconducting pairing. They could be related to the presence of a QCP at a critical doping close to the

optimal doping [35], where the T_c is maximal. To have a clear experimental picture of nematicity and determine the essence of its role is made particularly difficult since neamtic fluctuations appear to be intertwined with the magnetic ones mentioned above [36]; to further complicate this framework there is the cumbersome presence of the CDW, which dominate a big portion of the phase diagram, making the detection of nematicity a very difficult task. A good strategy, backed up by the suggested quantum criticality origin of nematicity, would be to look for nematic order in the superconducting phase, at a doping not far from p_{opt}. However, even in this case nematicity could be difficult to see, since it might be masked by the $d-wave$ superconducting order parameter: indeed, a signature - even vague - of a nematic pairing, i.e. a of nematicity in the superconducting state, is still missing.

Strain plays a crucial role in defining nematicity and CDW; strain does not simply induce a structural anisotropy which is then reflected in the measurements of physical properties; strain can also enhance nematicity, like a magnetic field would make the magnetic properties of a material with randomly oriented domains visible through macroscopic measurements. Recently it has been discovered that nematicity, induced by strain, can modify the Fermi surface of cuprates and therefore act on their charge modulations, modifying the electronic properties and enhancing the strange metal phase [37]. Playing a major role in influencing electronic properties and charge modulations, the nematic behaviour is believed to be a fundamental building block of the superconducting phase; as already said, its presence is not determined strain, whose role is to enhance it. This is confirmed by multiple scientific works, which showed the presence of "diagonal nematicity" [31], that is an anisotropy axis not oriented along the main cristallographic directions, which are the ones subjected to strain.

2 | Deposition and characterization of YBCO thin films

YBCO can be grown both in single crystal and in thin film form; in our work thesis we have employed the latter, in order to use the strain and confinement effects as additional degrees of freedom to modify the ground state.

YBCO is a really challenging material to grow in thin film form, since its structure is rather complex. Moreover, its properties are strongly dependent on the doping of oxygens, which are extremely volatile atoms, easy to diffuse out of the structure. Preserving pristine properties and the correct stoichiometry becomes even more challenging when thin films have to be patterned and/or shranck at the nanoscale.

In this chapter we will describe the process we have used for the deposition of thin films, both *c*- and *a*-axis oriented, together with the morphological, structural, and electrical transport characterization.

2.1. Thin film deposition

In literature there are mainly two methods, which have been employed for the deposition of YBCO thin films: they are high DC magnetron sputtering and pulsed laser deposition (PLD). We have used the latter one, mainly for the flexibility it offers to modify different deposition conditions, therefore spanning a large region of the phase diagram. Figure 2.1 illustrates the PLD system setup we have used to deposit the YBCO thin films.

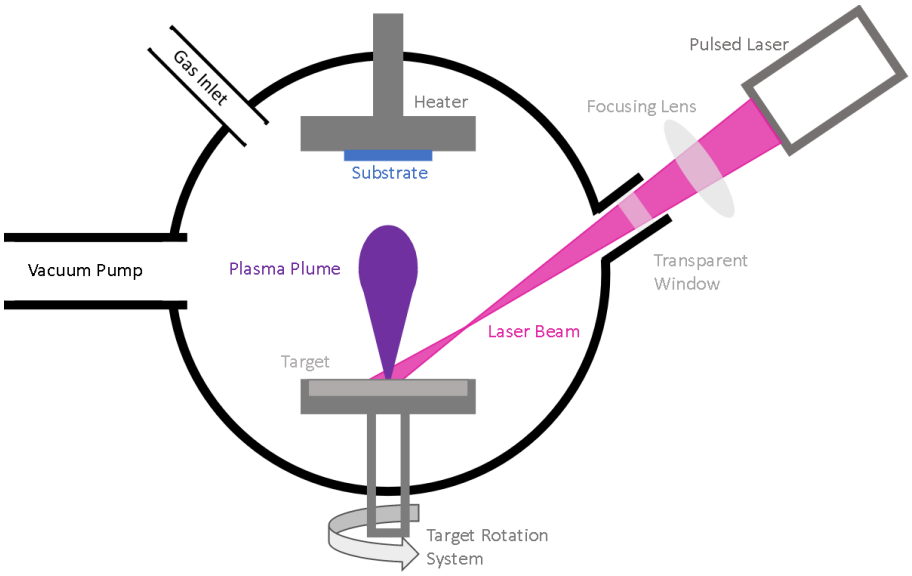

Figure 2.1: This is a sketch [38] of the PLD system we employed to deposit the films needed for our experiments. We have a main chamber, the turbo vacuum pump needed to reach an ultra high vacuum regime and a oxygen inlet to set the desired oxygen pressure in the chamber; there is the heater, on the bottom of which we place the sample holder during the deposition, and the material (YBCO) target positioned few centimeters underneath. On the target an excimer laser is focused which, thanks to its short wavelegnth and large fluence, is ideal for the ablation of a large amount of material (atoms, molecules, clusters, etc...).

the technique consists in the transferring, by means of an explosion, a certain amount of material from a target of the desired stoichiometry to a substrate. A laser is focused onto the target, its energy is absorbed and we have the formation of a highly directional plasma, the so called plume. PLD is fast, since the deposition rate is really high; thanks to the rapid removal rate following the explosion, atomic segregation on the target is not allowed, so the stoichiometry is preserved. The fast and intense heating of the target surface by the laser beam can provide a simultaneous evaporation of all the chemical components in the target, irrespective of their binding energies, preserving also the stoichiometry of the deposited material. Key parameters in this process are the laser fluence E and the pulse repetition rate f, which control the kinetics of the atoms in the plasma plume, influencing the nucleation and the growth of the thin film. YBCO is a very complex oxide and the background oxygen pressure P_d, in addition to controlling the plasma plume, helps in replicating the correct stoichiometry on the substrate. The distance between the target and the substrate d, together with the substrate temperature T_dep, affect the kinetics of the atoms impinging on the substrate and therefore the dynamics of the deposition.

High temperature allows for diffusion of the atoms on the substrate surface, which adapt to the underlying lattice and form crystalline grains with a specific direction. A steady post-annealing oxygen pressure P_{ann} helps in setting the desired hole-doping, oxygenating the film after the deposition.

2.2. Role of the substrate and strain effect

Thin films deposited by PLD grow epitaxially (from the greek words $\epsilon\pi\acute{\iota}$, which means 'upon' and $\tau\acute{\alpha}\xi\iota\varsigma$, which means 'arrangement') on top of a substrate, i.e. they grow in crystalline form with well-defined orientations with respect to the substrate. The choice of the substrate is therefore particularly important. The substrate acts as the platform, the cast, where the crystal structure of the film we desire to grow is built. It is therefore crucial that the lattice parameters of the overlayer material roughly match the ones of the substrate, in order to minimize the energy at the interface and avoid, in case of a notable mismatch, the formation of dislocations, which could be detrimental to the quality of the structure. We know that the superconducting and normal state properties of YBCO thin films can greatly differ from the ones in the bulk and, for this reason, a homogeneous and ordered growth is key to preserve these unconventional properties as much as possible. The main responsible of this potential modification is the strain induced by the biaxial stress due to the lattice mismatch between substrate and YBCO. The strain can be quantified by the following parameter:

$$\epsilon = \frac{a_s}{a_o} \tag{2.1}$$

where a_s is the lattice parameter of the substrate and a_o is the lattice parameter of the overlayer material; ϵ should in principle not exceed 10 percent if we want to ensure a sustainable epitaxial growth. The YBCO cell is orthorhombic and the choice of the substrate can affect the orientation of the deposited film, i.e. the twinning.

2.3. Twinning state

The YBCO unit cell is orthorombic and can be described by the three lattice parameters a, b and c, where $a = 3.82$ Å, $b = 3.89$ Å and $c = 11.68$ Å. If one uses a substrate with squared unit cell, which is the case of the most typical oxide materials used for the growth of YBCO, there will be a random exchange of the a and b axis: this causes an average in the plane of the macroscopic structural and physical properties of the film,

which loses the intrinsic orthorhombicity of the YBCO unit cell. The properties will be therefore, on average, the same along the two in plane directions. This has a crucial detrimental impact on the study of YBCO. For instance, considering transport properties, the resistivity is anisotropic, and lower along the b-axis direction, because of the presence of the chains along this direction, as discussed in previous chapter. In twinned films, the unidirectionality of the chains throughout the sample is lost, and the in-plane resistivity becomes isotropic. In order to minimize the random exchange of the two in-plane axis and therefore getting aligned unit cells with the same orientation next to each other, we worked on the substrate, both on the choice of material and the surface treatment, so to create the right conditions to have the desired structural growth. The path we followed implies the achievement of an in-plane anisotropic strain induced in the YBCO unit cell by the substrate.

2.4. c-axis oriented YBCO films on MgO(110)

To grow c-axis oriented YBCO we used [110] oriented magnesium oxide. MgO crystals are free from strain defects and have a thermal expansion coefficient similar to that of YBCO; this is important because if we deposit the film at high temperatures it can then experience large strain upon cooling to room temperature. MgO has a low dielectric constant (approximately equal to 10) and microwave losses, which make it suitable to be used in devices where a good coupling with the microwave radiation is required. MgO has a cubic symmetry, and when YBCO thin films are grown on its [001] oriented surface, twinned films are achieved. The [110] oriented MgO surface is rectangular with [001]=4.21 Å and $[1\bar{1}0]$=5.96 Å: this condition is not enough however to guarantee the growth of untwinned YBCO films.

2.4.1. Twinned YBCO films

For our experiments, we have first deposited a thin layer of YBCO on a non-treated MgO surface. After the deposition, we proceed with an annealing at a fixed oxygen pressure, whose function is to add oxygen atom into the CuO chains through the film, setting the desired doping.

A morphological characterization has been carried out through scanning Electron Microscope (SEM) and Atomic Force Microscopy (AFM). As we can see from fig. 2.2, the surface of the film is smooth, with clearly visible c-axis domains, which are characterized by a three-dimensional spiral-like growth. There are few holes and we can estimate the surface roughness to be around 1-2 nm (see fig. 2.6, a).

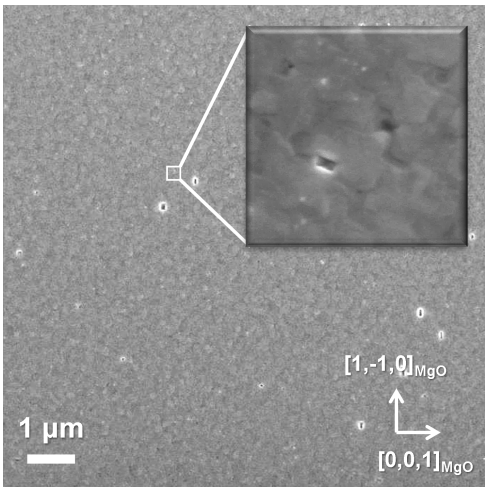

Figure 2.2: This is a SEM image of the surface of a twinned YBCO films. In the zoomed panel we can have a closer look at the characteristic spiral-like nucleation of the *c*-axis domains.

X-Ray Diffraction (XRD) is a valid tool to provide information about the cristallinity of the structure, revealing the regularity of the YBCO epitaxial growth. In this case we use instead a symmetric $2\theta - \omega$ scan, in which we can see the 00n Bragg's reflections, which indicate a fully *c*-axis oriented growth.

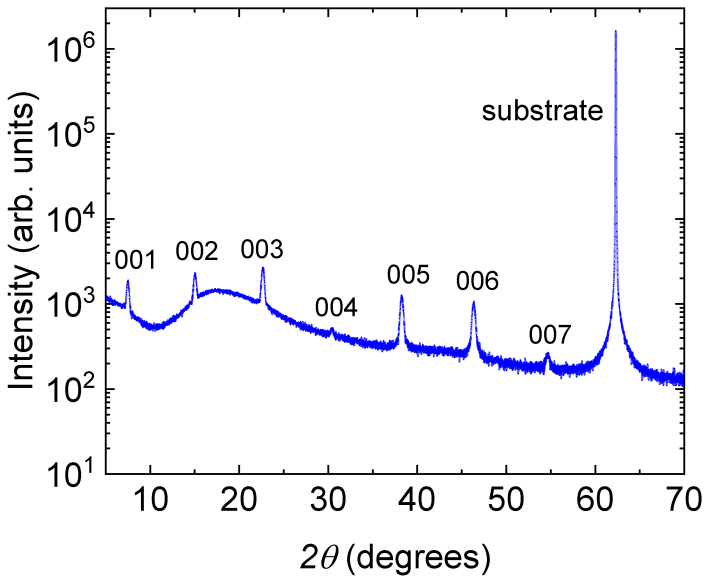

Figure 2.3: XRD symmetric scan, where the (00n) Bragg reflections are an indication of the out-of-plane *c*-axis.

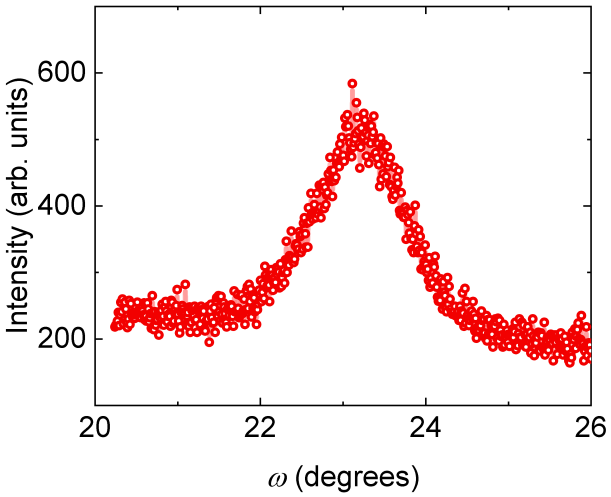

Figure 2.4: XRD ω scan (rocking curve), carried out in correspondence of the (006) peak of YBCO. The width of the rocking curve provides information about the mosaicity of the film.

By applying Bragg's law, from the 2θ position of the peaks we can derive the c-axis length, from which we can infer information about the strain and the doping. One of the consequences of the presence of the oxygen atoms, which are added in the $a-b$ planes, is to reduce the c-axis length to preserve the total volume of the cell: for this reason the higher the doping, the smaller the length of the c-axis. Also the strain can be inferred from the determination of the c-axis length: the measured c-axis is longer than in the unstrained case, from which we can determine that YBCO films grown on MgO (110) are subject to an in-plane compressive strain. We also carried out an ω-scan (rocking curve, see fig. 2.4) in correspondence of a (00n) reflection, which shows a rather sharp peak; the width of the Bragg peaks in ω can be related to the mosaicity of the film, which is the degree of alignment between different crystal grains. The narrow peak we see in 2.4, gives us once again insight of the good crystallinity of the films.

To get an accurate estimation of the twinning degree, XRD characterization is also needed. From the (308)-(038) asymmetric map (see fig. 2.5) we see the presence of two distinct peaks, which can be directly associated to the presence of a-axis (308 peak) and b-axis along one direction. Being able to distinguish between two different peaks give us information about a poor degree of untwinning, which reflects itself on a mixing along both the two in-plane direction, of a-axis and b-axis components.

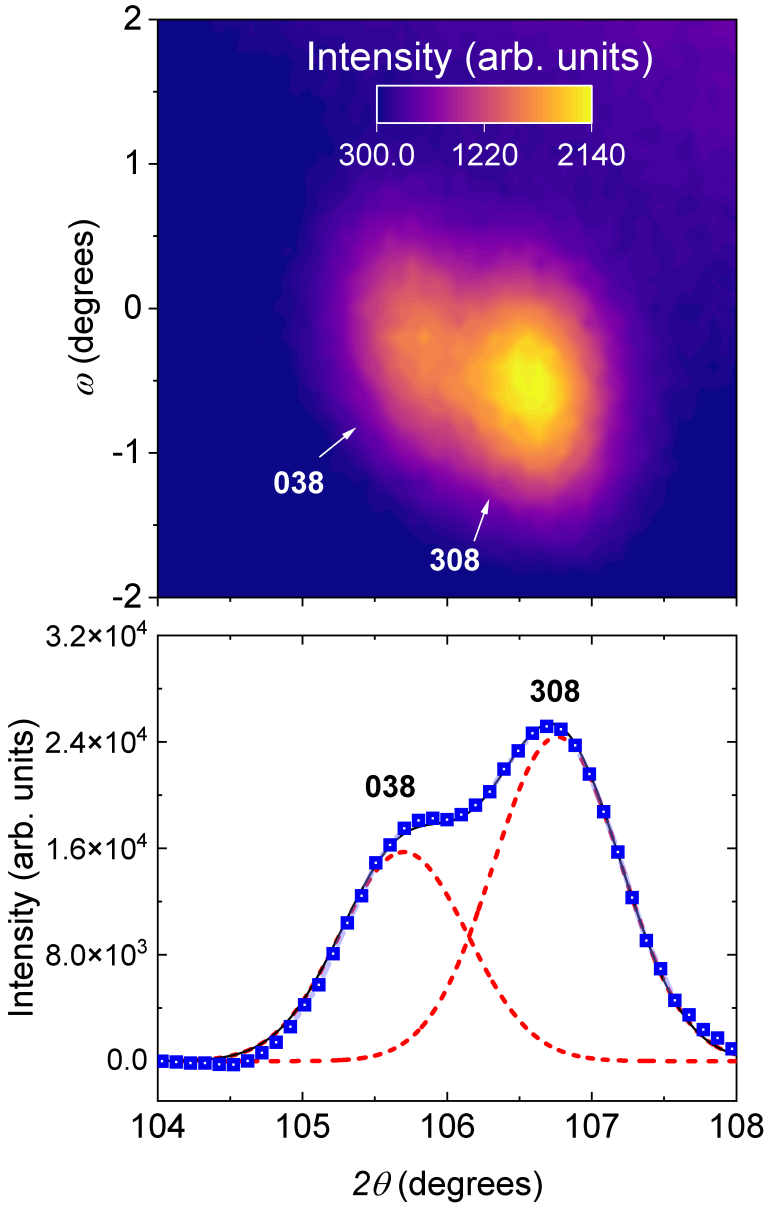

Figure 2.5: In the top picture we have a asymmetric 308-038 map, which shows us the presence of two distinct peaks, one referring to a-axis and the other to b-axis components. This map points therefore to a poor degree of untwinning, in which there is a marked mixing of the two in-plane directions. In the bottom picture we have a two peaks fit of the asymmetric map; we have the two gaussian-like peaks associated to the two different crystallographic components plotted with red-dashed lines, the sum of the two curves with solid black line and the actual data coming from XRD measurements indicated with blue dots. We can see that we have almost complete superposition of the line of the fit with the real data points, confirming the validity of the fitting procedure.

2.4.2. Untwinned YBCO films

Figure 2.5 shows how the choice of the substrate and the deposition procedure described in the previous section are not enough to produce untwinned YBCO films. First of all, the [110] MgO orientation would allow for the growth of untwinned YBCO only if the in-plane substrate lattice parameters were close to the ones of YBCO. The strain induced by the MgO substrate on the overlaying YBCO films is peculiar and very small because of the notable mismatch between the in-plane lattice parameters (δ^n is roughly equal to 9 and 35 along the [0,0,1] and [1,-1,0] MgO directions respectively). In order to induce strain on the YBCO films and suppress the twin pairs we nanostructured the MgO surface aiming at introducing additional asymmetry in the substrate, and therefore inducing an anisotropic strain into the film (see fig. 2.6, b) [39]. The surface reconstruction has been obtained through a heat treatment consisting in 5 hours of $in-situ$ annealing, at the same oxygen pressure employed in the deposition of the YBCO films and at a temperature T_{preann} slightly higher than T_{dep}.

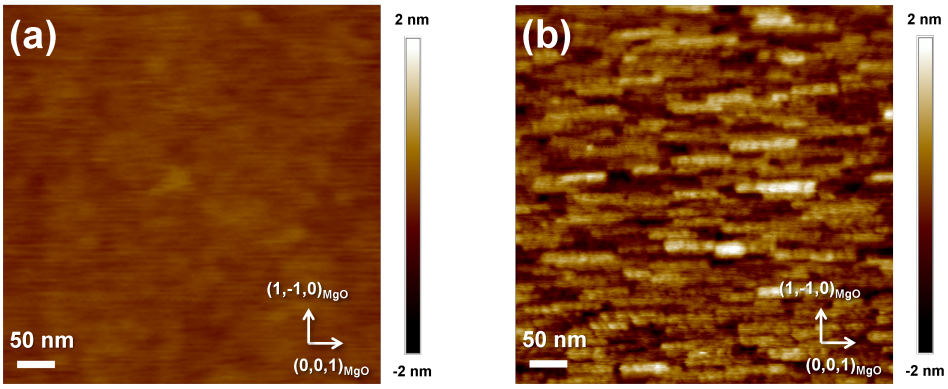

Figure 2.6: AFM picture of a YBCO thin film; from it we can have a clear visualization of the morphology of the surface and we are able to get information about the roughness. In panel (a) we have the AFM image of the substrate taken before the 8h annealing process, whereas in panel (b) we can clearly see the impact of this annealing technique on the substrate surface morphology, with the appearance of elongated facets along the [100] direction.

Such surface treatment does not by itself guarantee the achievement of untwinned YBCO, since the epitaxial growth of YBCO thin films is not solely influenced by the substrate morphology. If we want to get a proper degree of untwinning, we must act on the different deposition parameters in order to find conditions able to favour this peculiar arrangement of the YBCO unit cells. In particular, the relative position of the substrate with respect to the plasma plume is also crucial. We have therefore optimized the growth of YBCO

on the MgO substrate, by depositing different films and changing each time the substrate position. In particular, we have tried to use an off-set position, with the center of the plume misaligned with respect to the center of the substrate: in this way, the film grows in a diffusive regime. The ablated material, when in contact with the substrate, will be subject to a different dynamics, which will modify the strain induced by the substrate, producing a different strain: this might therefore favor a different twinning state (see fig 2.10).

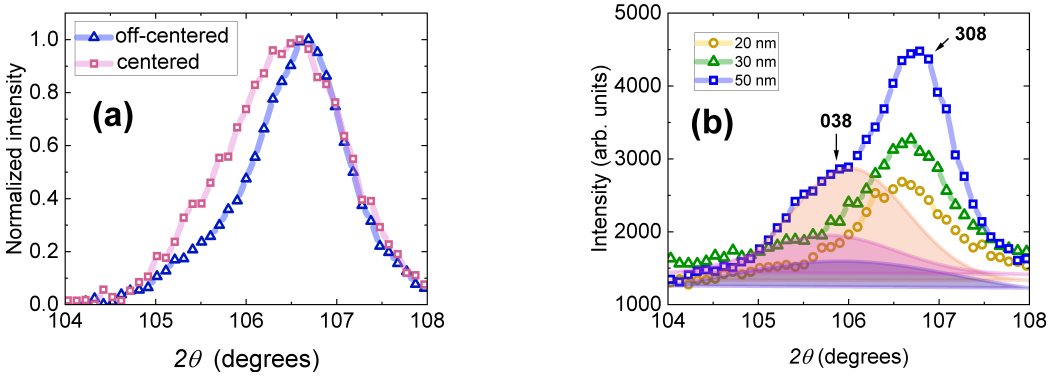

Figure 2.7: In panel (a) we can see a comparison between two normalized XRD omega scans taken from the 308-038 asymmteric maps of two different 30 nm thick YBCO films. The blue line corresponds to a film deposited in a off-centered position of the sample holder with respect to the plume, while the pink line corresponds to a film deposited with the plume almost in line with the position of the substrate. As we can see, an off-centered condition improves the untwinning degree of the film. Indeed, its corresponding ω-scan presents a less marked presence of the peak associated to the second in-plane axis, deducible from a curve which is more symmetric. In picture (b) we can observe the effect of the thickness of the film on the untwinning; the thinner the film, the better the disentanglement of the two in-plane components. Nevertheless, it is worth mentioning that the untwinning does not seem to be proportional to the thickness: while going from 20 nm to 30 nm thick films we do not observe a notable increase of the twinning, moving to a 50 nm thick film we see an abrupt appearance of the peak associated to the other axis (highlighted with the light red curve), indicating how there could be a sort of thickness threshold above which we have a marked degradation of the untwinning level.

By setting a fixed oxygen pressure after the deposition, we obtained films with the desired level of doping (the parameters of the deposition are listed in table 2.1).

	T_d	P_d	d	E	f
***c*-axis films**	760 °C	0.8 mbar	55 mm	2 J/cm2	6 Hz

Table 2.1: In the table are listed the most relevant parameters used for the deposition of *c*-axis oriented and untwinned YBCO thin films.

The thickness of the film might also play a major role in the overall untwinning of the deposited film. We have discussed indeed previously about how the strain is a crucial factor for the achievement of untwinned films. But the strain induced by the substrate is reduced, when the thickness of the film is increased.

To investigate the relation between strain, thickness and untwinned degree, we have grown YBCO thin films with different thicknesses in the range between 20 and 50 nm, all in the same deposition conditions. As we can see in the picture 2.7(b), for 20 and 30 nm thick films XRD 308-038 asymmetric maps show the presence of two peaks, one much more prominent than the other, indicating a very good degree of untwinning, almost reaching 90%. This is among the best results achieved for YBCO thin films. However, the untwinning degree abruptly degrades when the thickness of the films in increased from 30 to 50 nm thick films.

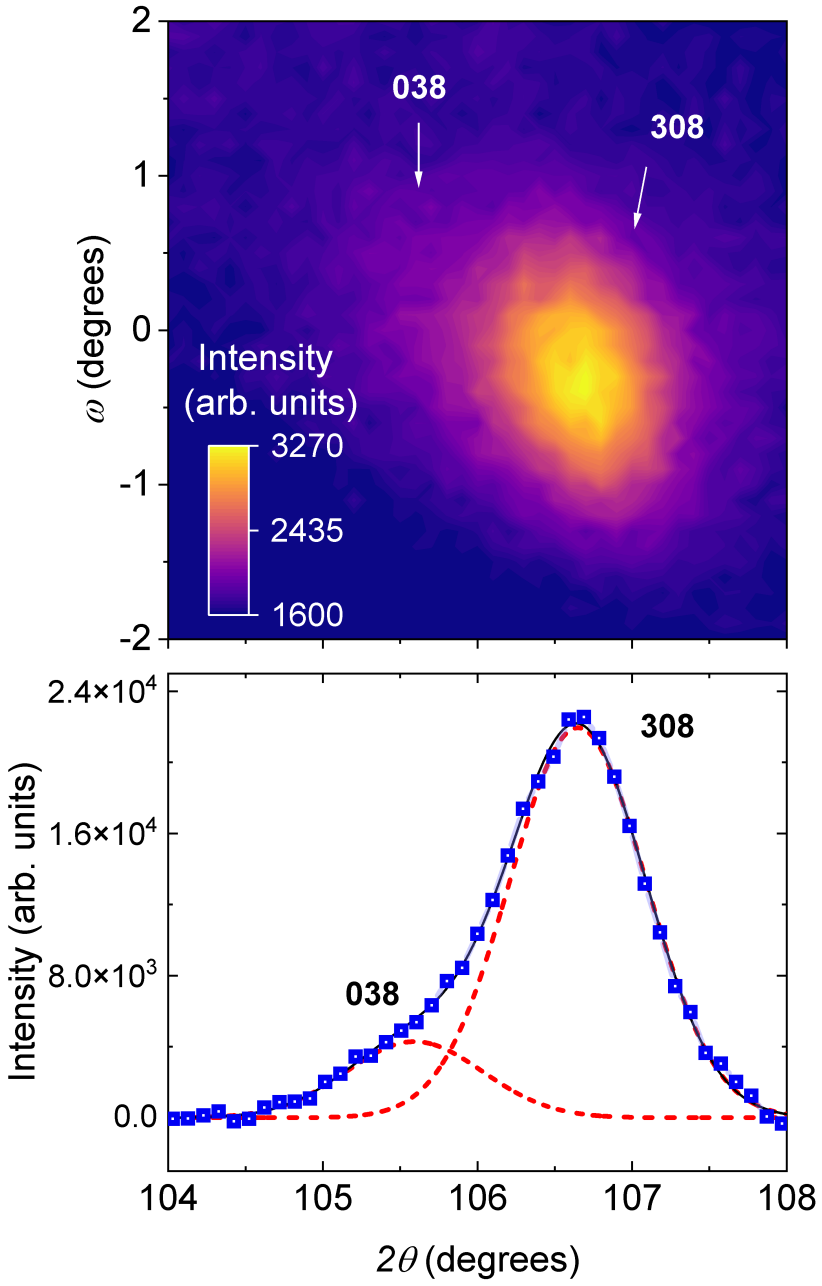

Figure 2.8: 308-038 asymmetric map, showing almost the exclusive presence of the 308 peak, indicating a good degree of untwinning. In the bottom picture we have the same fit described before, from which emerges a limited presence of the peak associated to the *b*-axis component.

The SEM pictures of untwinned films (see fig. 2.9) present 1 nm deep elongated channels, oriented mainly along the [110] direction of the substrate, which would correspond to the YBCO *a*-axis. This anisotropy in the morphology of the surface confirms the presence of

a structural anisotropy due to the untwinning.

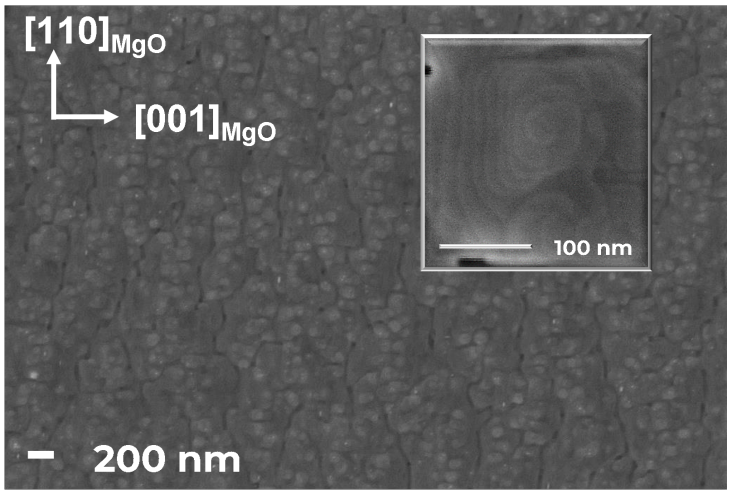

Figure 2.9: This is a SEM image of the surface of a twinned YBCO films. In the zoomed panel we can have a closer look at the characteristic spiral-like nucleation of the *c*-axis domains.

Transport measurements are a very effective way to characterize YBCO thin films. A resistance versus temperature $R(T)$ curve provides information regarding the superconducting properties of the film, like the superconducting critical temperature, in addition to some insight on the doping and the overall structural quality of the film. A sharp superconducting transition is, for instance, one of the best benchmarks of the homogeneity of the film. To check the untwinning state of the films, we have performed measurements along the two cristallographic directions adopting a Van der Pauw configuration [40]. The range of temperatures along which we could perform the measurements goes from 4.2 to 300 K, even though for overdoped and slightly underdoped films the lower temperature limit in the $R(T)$ curve was set to be higher.

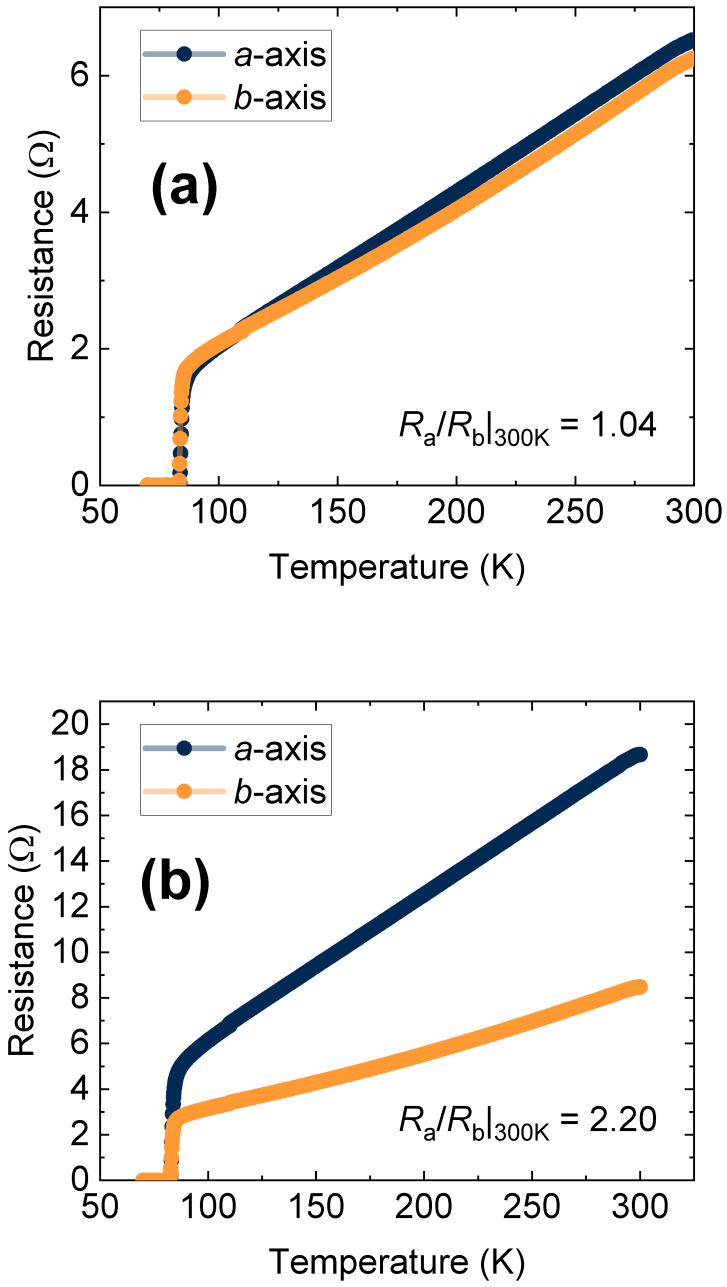

Figure 2.10: In picture (a) we can see the $R(T)$ curves measured along the two in-plane axis in the case of a twinned sample, 50 nm thick. The two resistances are in fact very similar, with a ratio which is equal to 1.04 at 300 K. The sample is not perfectly twinned, there is a slight prevalence of chains along one direction, but still the properties are much more isotropic than what is expected in bulk, untwinned, material. In picture (b) we have instead the resistance versus temperature in the case of an untwinned sample, 30 nm thick; we can observe a clear anisotropy of the two resistances along the a and b axis, with a much higher conductivity along the latter (2.20 times higher at room temperature).

As we can see in the picture, in the twinned film the resistance is roughly the same along the two directions, indicating that in both directions we measure an average of the a-axis and b-axis contributions. In the untwinned sample we witness a clear difference in the resistance along the two in-plane axis: a and b components are mostly decoupled and the presence of the oxygen chains in the b direction translates in a clearly lower resistance, with a parabolic-like behavior of the resistance at high temperature. The anisotropy we measure in these films is of the same order as the best untwinned YBCO single crystals [24].

Underdoped films

As already stated before, the main goal of the active research in cuprates and specifically of this work is to explore their phase diagram and investigate the forms of order that characterize it. In order to do so, it is of course fundamental to be able to vary in a controlled and reproducible way the doping of the YBCO films. Obtaining slightly overdoped films is relatively easy: they are fully oxygenated and realized using an almost atmospheric oxygen pressure in the deposition chamber during the postannealing [41, 42]. Going instead to the underdoped is not as straightforward: a careful procedure has been however developed at Chalmers to succeed in this task [43]. In order to get good quality underdoped films we proceeded, immediately after the deposition, with an $in-situ$ post-annealing at a fixed and steady pressure. It is a matter of extreme importance that the pressure stays constant throughout the whole post-annealing process, until we reach room temperature; this is because pressure instabilities can be very detrimental to the final degree of oxygenation of the film, causing a broad and irregular transition. In fig. 2.11 we can the $R(T)$ curve typical of underdoped films.

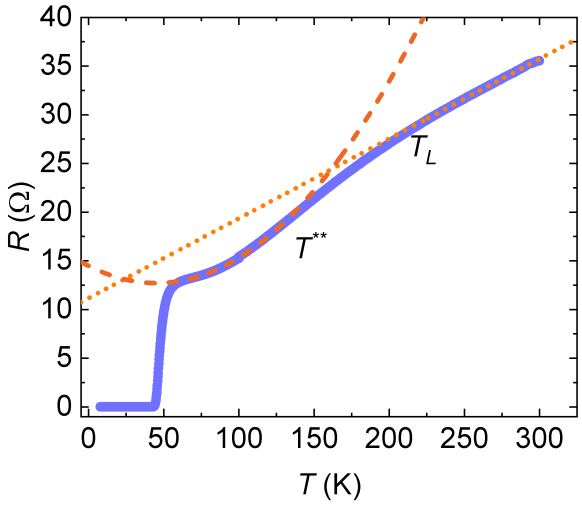

Figure 2.11: $R(T)$ curve of an underdoped c-axis oriented YBCO film. At high temperature we can identify a regime in which we have a linear resistance, characteristic of the strange metal phase. T_L, the temperature at which we lose this linearity marks the end of the end of the strange metal and its value is close to the pseudogap temperature T^*. The T^2 dependence of the resistance is recovered at T^{**}, and it can be seen as a restoration of the Fermi liquid behavior in the underdoped region.

Determination of the doping

If we want to construct a proper phase diagram we have to determine the doping of our films starting from the information we can get from transport and XRD measurements, which are mainly the T_c and the length of the lattice parameters. A common approach to estimate the doping is to use the following parabolic relation:

$$1 - T_c/T_c^{max} = 82.6 \cdot (p - 0.16)^2 \tag{2.2}$$

where T_c^{max} is the T_c at optimal doping. However the trend of the T_c as a function of the doping is not perfectly parabolic, with a deviation from it around $p = 1/8$, where we have a depression of the T_c due to the presence of strong CDW. The length of the the c-axis increases monotonically as we move to the lower dopings and if we carry out an interpolation of our data with the two methods we can get an accurate estimation of the doping level of our films [25].

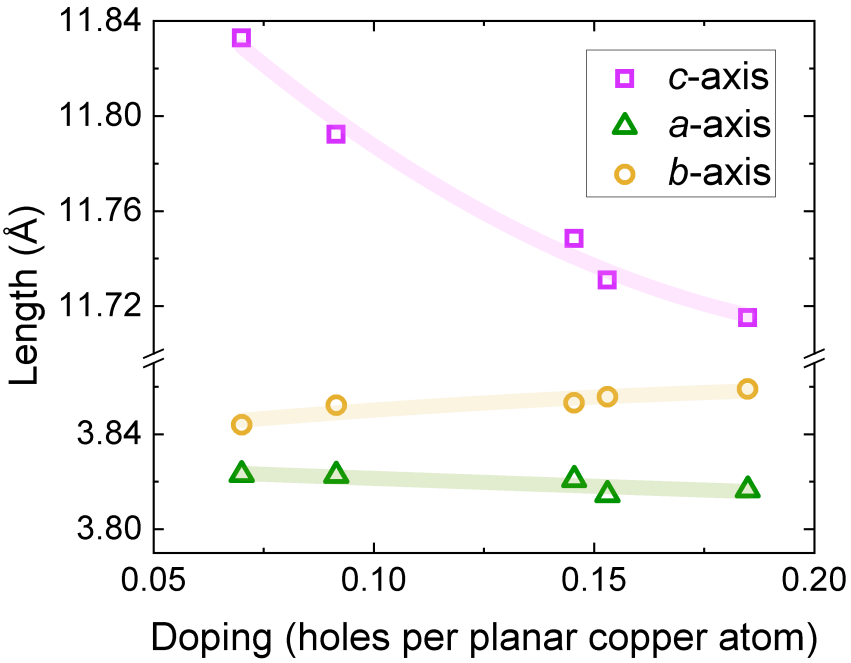

Figure 2.12: In the picture we can see the evolution of the lattice parameters as a function of the doping. We have that both c-axis and a-axis monotonically increase, while the b-axis decreases. Those trends are due to the presence of the oxygen: it is responsible of holding the YBCO cell structure together and is located along the b-axis; going in the underdoped regime and therefore removing it, causes a contraction of the b-axis while at the same time producing an expansion of both c and a-axis.

2.5. a-axis oriented films

The growth of a-axis oriented films is in general more complicated than in the c-axis counterpart. The lower temperature employed in the deposition does not help a proper nucleation of a-axis grains, resulting in poor cristallinity of the final film and in a lower transition temperature. To favor the growth of a-axis oriented films, a process has been developed at Chalmers [44], where the YBCO is grown on top of a rf sputtered, 90 nm thick, layer of PBCO. This film, acting as a buffer layer, is deposited on a $SrLaGaO_4$ substrate. After the deposition of this buffer layer, which is known to promote the growth of homogeneous a-axis superconducting films with high crystallinity, the sample is transferred $in-situ$ to the pulsed laser deposition chamber. Here, a YBCO film, with a thickness of 50 nm is deposited. By slowly increasing the temperature after the deposition, we achieve slightly overdoped films, where the CuO chains are fully oxidized. The

parameters of the deposition are listed in table 2.2.

	T_d	P_d	d	E	f
***a*-axis films**	805 °C	1 mbar	55 mm	2 J/cm2	6 Hz

Table 2.2: In the table are listed all the most relevant parameters used for the depostion of YBCO c-axis oriented untwinned films.

A thorough X-ray Diffraction (XRD) analysis has been performed to determine the structural properties of the $ex-situ$-annealed underdoped a-axis films. The symmetrical $2\theta-\omega$ scans confirm what has been previously observed on the as-grown, fully oxygenated films, i.e. that the films are highly crystalline and a-axis oriented, with a negligible contribution coming from possible c-axis oriented grains.

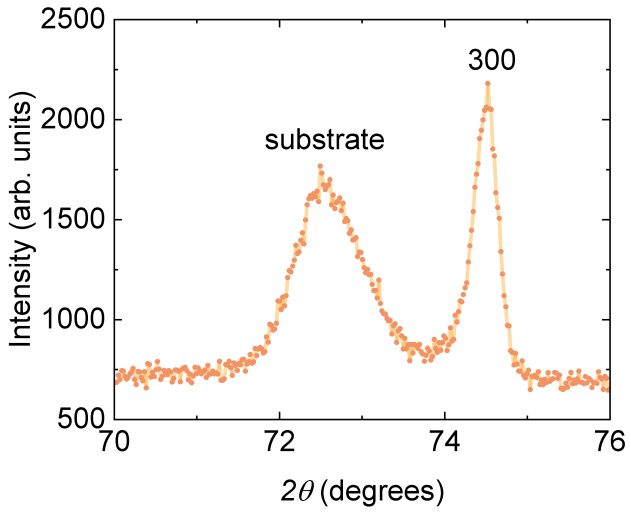

Figure 2.13: $2\theta-\omega$ scan. The 300 peak of the YBCO accompanied by one other peak, corresponding to the 300 of PBCO. We cannot observe other peaks, which implies the YBCO film is purely a-axis oriented. If there were b-axis domain, in fact, we would have observed a further peak, coming from the 030 reflection, located at smaller angles with respect to the 300 peak, being the b-axis always greater than the a-axis. Same thing can be said for the 009 reflection, related to c-domains, which would be located in the same range of angles; its absence is again a sign of a pure a-axis nucleation of the film.

In fig. 2.13 we have the $2\theta-\omega$ scan carried out from 70 to 76 degrees, around the YBCO 300 reflection; at intermediate angles between these two we cannot see a clear third peak,

which would be (030) YBCO reflection, associated to the b-axis: there is almsost none random exchange of a and b axis, i.e. we have a sample structure in which the dominant out-of-plane component is the a-axis. In addition to the symmetric scan, we carried out an asymmetric maps around the (038)-(308) YBCO reflections (see fig. 2.15) and we could identify one single peak, verifying the excellent degree of untwinning of the films. As previously done in the case of c-axis oriented films, the morphology of the film has been investigated with SEM (see fig. 2.14).

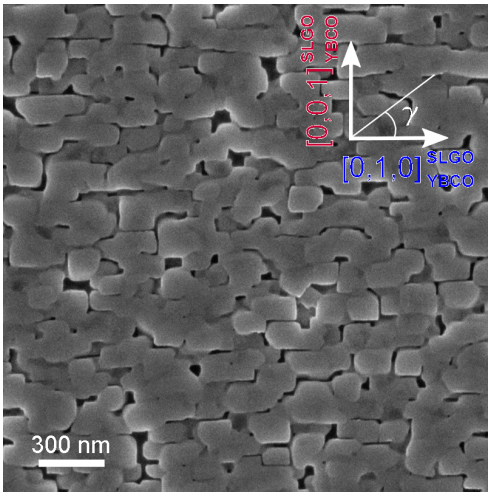

Figure 2.14: SEM picture of the surface of a a-axis oriented film. We can observe a granular structure with elongated domains, typical of a-axis films.

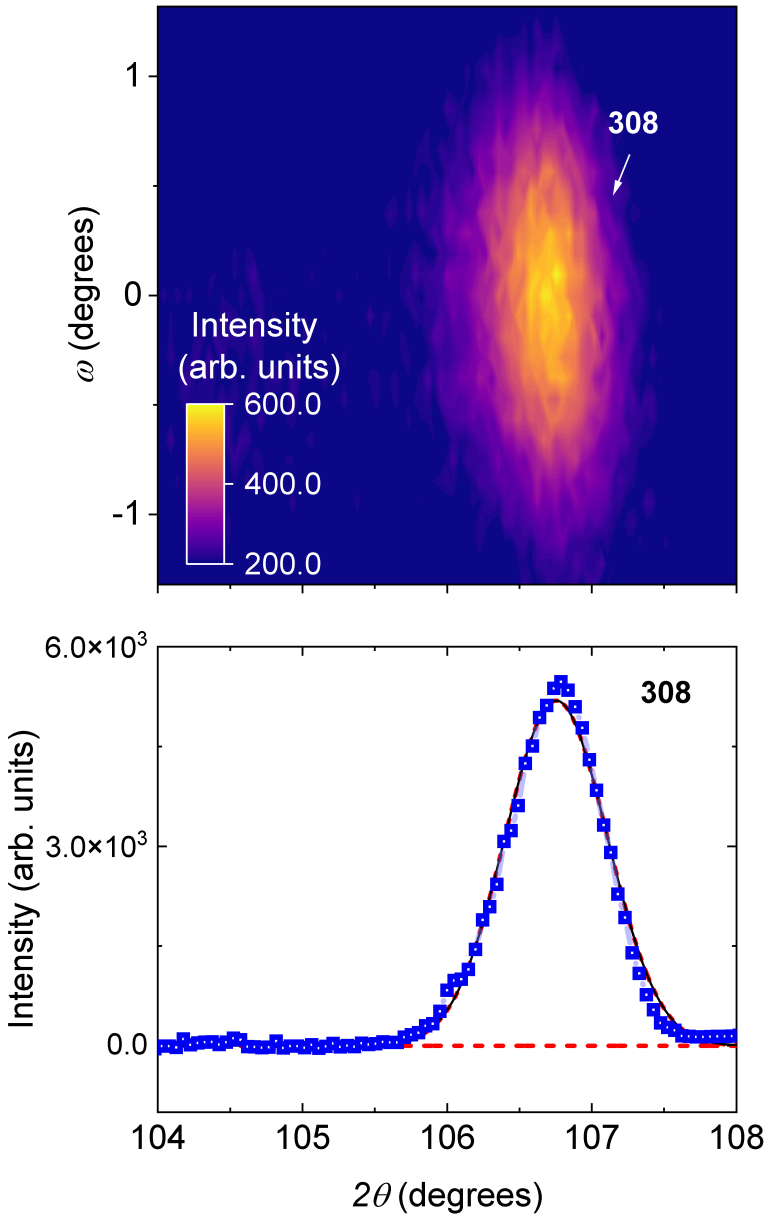

Figure 2.15: (a) Asymmetric 308-038 map, where we can clearly see the presence of one single, peak, associated to the sole presence of the *c*-axis component. (b) Fit of the integrated intensity of panel a, in which we can see the absence of a *b*-axis associated peak.

As we can see from the picture, the surface shows by a granular texture, with the elongated domains typical of the a-axis films aligned along the [010] direction of the film (*b*-axis). SEM allows you also to get an insight on the transport properties of the surface, since charging effects, which produce really bright images, are a sign of poor conductivity.

3 | Nanofabrication

The main goal of this work is the study of nanoscale ordering in HTS through transport measurements on YBCO nanostructures. In order to achieve such goal is crucial to fabricate devices that retain as much as possible the properties of the bulk, which we already worked so hard to maintain through a thorough optimization of the thin film deposition parameters. This challenge is to fabricate devices without degrading the film's normal superconducting properties [45] [46] [47] [48]. The task is made particularly difficult by the chemical instability of YBCO and by its really short superconducting coherence length ξ, which make the final structures extremely sensitive to structural inhomogeneities. Our group has developed and used for over a decade a fabrication method to overcome these problems and fabricate pristine nanowires with record high J_c [49–52], method that will be described in the following section.

3.1. Nanopatterning procedure

The nanofabrication routine consists mainly of one-step electron beam lithography in combination with a carbon hard mask and a very gentle argon ion milling. This method has been optimized for the fabrication of YBCO nanostructures [49–51], and also showed to be reliable for other cuprate compounds as $Pr_{2x}Ce_xCuO_{4\delta}$ (PCCO) [53] and $La_{2x}Sr_xCuO_4$ (LSCO). The nanostructures, whose lateral dimensions have been shrank down to 50 nm, preserve both in the normal and in the superconducting state the properties of the starting thin films. In particular for YBCO, the nanowires have shown high critical current densities, close to the depairing limit, and critical temperatures which are unchanged with respect to the unpatterned thin film [54]. For their characteristics, they have been already successfully employed in several devices, where nanoscale elements are needed, as single photon detectors [55, 56] and superconducting quantum interference devices [57, 58].

The nanofabrication steps are the following:

1. Deposition of untwinned YBCO thin film via PLD.
2. Gold capping of the YBCO thin film. We start with an $ex-situ$ evaporation of a

60 nm thick gold layer on top of the YBCO film, which will protect the film from contaminations and help the thermalization of the forming nanostructures during the etching process, therefore limiting oxygen out-diffusion.

3. The gold capping is immediately followed by the deposition of the hard carbon mask. The carbon mask is deposited via PLD through three steps of increasing energy of the laser. At first the relatively low energy of the laser favours the growth of graphite-like carbon, which better adheres to the gold surface; then, increasing the energy, we obtain a more diamond-like carbon, ensuring the structural resistance of the final mask. We have then the spinning of the resist. We span on the carbon mask two different resists, with two different sensitivities to the electron beam.

4. The nanowire geometry is defined by Electron Beam Lithography. We then remove the exposed area during resist development.

5. A thin layer of chromium is evaporated on top of the double layer of resist, and will act as a mask for the carbon.

6. The carbon mask is defined after the chromium is lifted off.

7. The carbon layer which is not covered by chromium is removed by low power oxygen plasma etching.

8. The Cr layer, the Au and YBCO which are not covered by C, are etched by Ar^+ ion-beam milling. The sample to be etched is placed on a stage which is cooled down with liquid nitrogen during the all process. As already mentioned, YBCO is chemically unstable and high temperature would make it susceptible to oxygen out-diffusion; this could turn out to be very detrimental to the final nanowires superconducting properties and, in the case of underdoped YBCO, even make the wires insulating. The heat generated by the impact of the highly energetic argon ions on the sample is then potentially harmful: therefore the presence of the cooled stage and the gold capping, as well as an appropriate choice of the etching parameters (the current and beam voltage values are the lowest allowing the etching of YBCO) ensure the minimization of the damages caused by the ions to the nanostructures.

9. The remaining carbon, which has an etching rate much lower with the respect to the one of the YBCO, therefore resisting during the Ar^+ ion-beam milling, is then removed by plasma etching, while the gold layer is kept.

All the aforementioned steps are sketched in fig. 3.1.

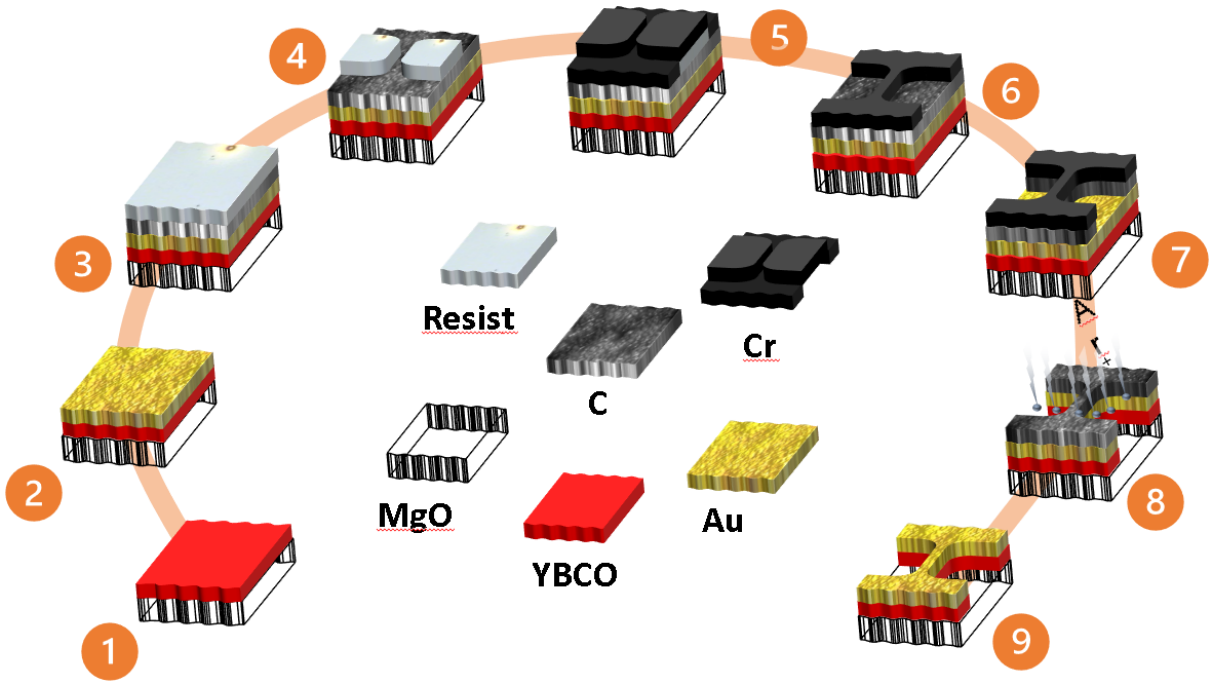

Figure 3.1: This is a sketch of the steps involved in the fabrication process [59].

A SEM image of a nanowire taken at the end of the fabrication process is instead shown in fig. 3.2.

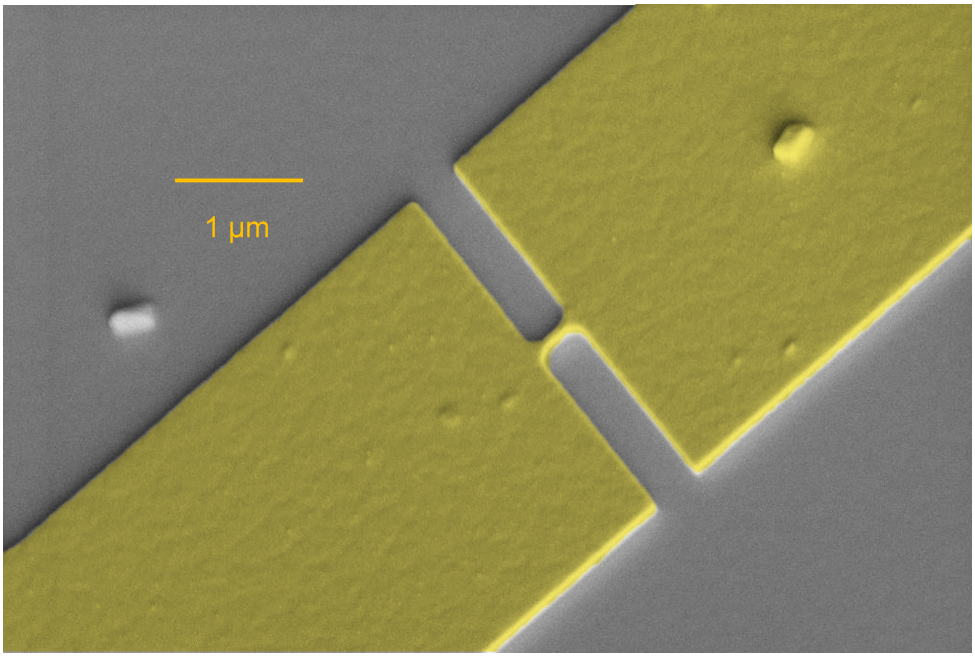

Figure 3.2: Coulorized SEM picture of a nanowire.

4 | Confinement by patterning to study nematicity

In this chapter we will present the measurements and the results of the first approach we adopted to shed light on the complex intertwining of orders we have in the phase diagram of cuprates. More specifically, we aimed at investigating the nematic order within the superconducting state with the help of transport measurements at cryogenic temperatures in YBCO nanowires. Here, the confinement of the CuO_2 planes is obtained through nanopatterning. This strategy can be effective in shedding lights on nematicity mainly for two reasons: first, the thickness of the wires is on the order of the nanometer, the same order of magnitude of the fundamental length-scales of superconductivity, which makes the transport highly directional; second, the results of transport measurements at cryogenic temperatures can shed light on the coupling between nematicity and Cooper pairs, a link which is still missing so far.

4.1. Nematicity in YBCO nanowires

The first of the two main goals of the thesis work is to investigate the angular dependence of the in-plane J_c employing YBCO nanowires.

To design the experiment, we have first chosen to pattern YBCO films whose hole doping level is about $p = 0.19$, i.e. slightly overdoped films. In the underdoped case, the low amount of oxygen introduced by doping is randomly distributed along the b-axis direction of the CuO planes, causing inhomogeneities at the nanoscale in the transport properties and therefore potentially high fluctuations in the J_c values; in overdoped films the CuO chains are overall present with more regularity throughout the sample, allowing for more stable J_cs.

A second parameter we took into account when designing the experiment was the film thickness. As previously discussed, strain on few-unit-cell thick films ($\approx$ 10 nm) plays a very important role in making the nematic order stand out [37]. However, the strain

induced by the substrate tends to become weaker if we increase the thickness of the film: by previous experiments, we know for instance that 50 nm thick films are already partly relaxed. At the same time, reducing too much the thickness could amplify the fluctuations of the J_c values [42]. As a compromise, we have opted for using films whose thickness is 30 nm.

A third crucial parameter to consider is the twinning state of the films. We have to pattern untwinned films, so to preserve the structural anisotropy of YBCO in bulk form, from which anisotropic transport properties derive.

Finally, we have to pattern nanowires on these films with a certain width w. We opted for fabricating nanowires with two different width: $w = 100$ nm, and $w = 300$ nm; in the former case nematicity effects are supposed to be enhanced, but at the same time the reduced width makes them extremely susceptible to fabrication defects and therefore amplifies J_c fluctuations. Wider wires allows in principle for more stable J_c values, still not denying the possibility to observe nematic fluctuations of the critical density current.

Before investigating the nematic state, which is associated to an unexpected, additional anisotropy of the transport properties, we have to check if the expected anisotropy in the transport properties can be probed in the nano-system which we aimed to be the focus of our investigation. Indeed, in untwinned YBCO single crystals and thin films an in-plane anisotropy of the superconducting properties is present, mainly due to the orthorhombicity of the crystal structure and the presence of the b-axis oriented CuO chains. In order to verify the presence of this anisotropy contribution we decide to pattern first on a 30 nm thick overdoped YBCO film nanowires oriented exclusively along the two main in-plane crystallographic directions, i.e. the a and b axis.

From now on, for the sake of simplicity and of an easier comprehension of the measurement data, we will use the convention to assign to the b and a axis the angles 0° and 90°, respectively.

4.1.1. Nanowires at 0 and 90 degrees

In principle a structural anisotropy, such as the one introduced by the untwinning, should reflect itself on a London anisotropy, which translates into having different London penetration lengths along the main crystallographic directions. Indeed, the Ginzburg-Landau formula for the theoretical depairing current value is the following,

$$J_d = \frac{\Phi_0}{3^{3/2}\pi\mu_0\lambda_0^2\xi_0} \tag{4.1}$$

showing how the value of the λ has a strong influence on the J_c. This is the reason why we expect that the anisotropy of the film would produce an anisotropy in the J_c values. The first step of our experiment was aimed therefore at observing different J_c along the a and b axis. We only patterned nanowires at 0 degrees (oriented along the b direction) and at 90 degrees (oriented along the a direction). In order to observe the expected anisotropy was crucial to collect as much measurement data as possible, so that a large statistics could shield the final results from the unavoidable J_c fluctuations and allow us to see the effects due to the intrinsic physics at play. We patterned a total of 176 nanowires, 88 for each of the two chosen widths, equally divided among the 0 and 90 degrees directions. All the measurements have been carried out at a temperature of 4.2 K, so that we could study the nematic behavior in the superconducting state. As mentioned before the footprints of nematicity have been observed - with some exceptions [32, 37] - mainly in the pseudogap region; our intent was to look for nematic evidence also in the superconducting phase in order to suggest a nematic behaviour of the Cooper pairs.

We have measured the current voltage (IV) characteristic of each wire, from which we can extract the critical current I_c.

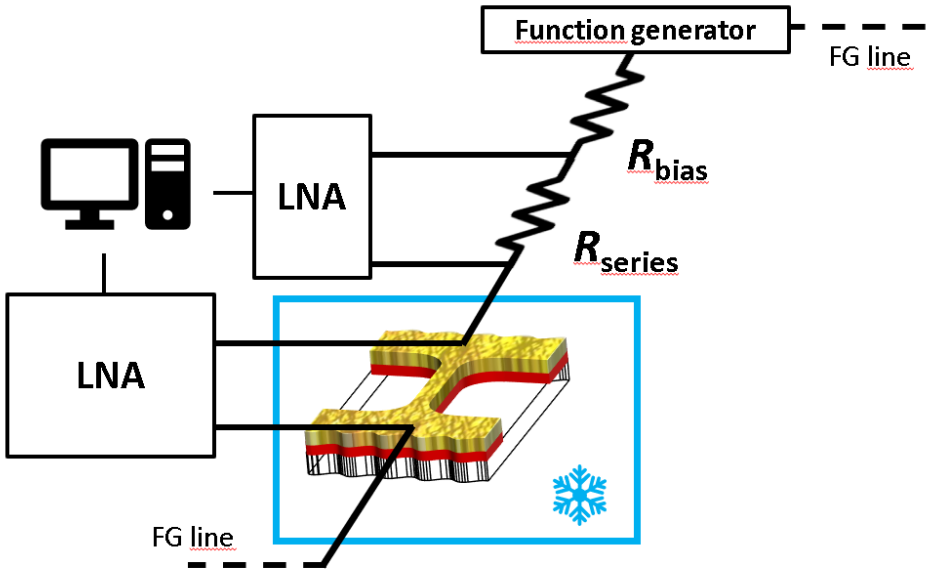

Figure 4.1: Sketch of the measurement setup. The nanowire is cooled down at T = 4.2 K with liquid helium and with two contacts at its extremities we apply a current determined by the bias resistance. With the help of other two contacts we read the voltage drop occurring through the wire and combining it with the voltage drop through the series resistance we obtain the I-V characteristic of the nanowire.

The I_c is the value of the current flowing through the wire beyond which we observe an increase in voltage, that is the current value needed to kill the superconducting state. Knowing the thickness t of the film and the width w of the wires patterned on it, we could easily derive the J_c values of each wire, as $J_c = I_c/(wt)$.

We measured the IV of all the nanowires, which were all working: this proves the effectiveness of the fabrication method. For every width and every orientation, we have a population of measured J_c, of which we have determined the average along with the standard deviation of the distribution. These two quantities (the latter in form of error bar) are plotted in figure 4.2 as a function of the angle for the 0 and the 90 degrees distributions, at each of the two different widths. Here, the values for the -90 degrees direction are the same derived for the 90 degrees orientation, since the two are physically equivalent; we represented them in order to provide a clearer and symmetric visualization of the J_c values anisotropy.

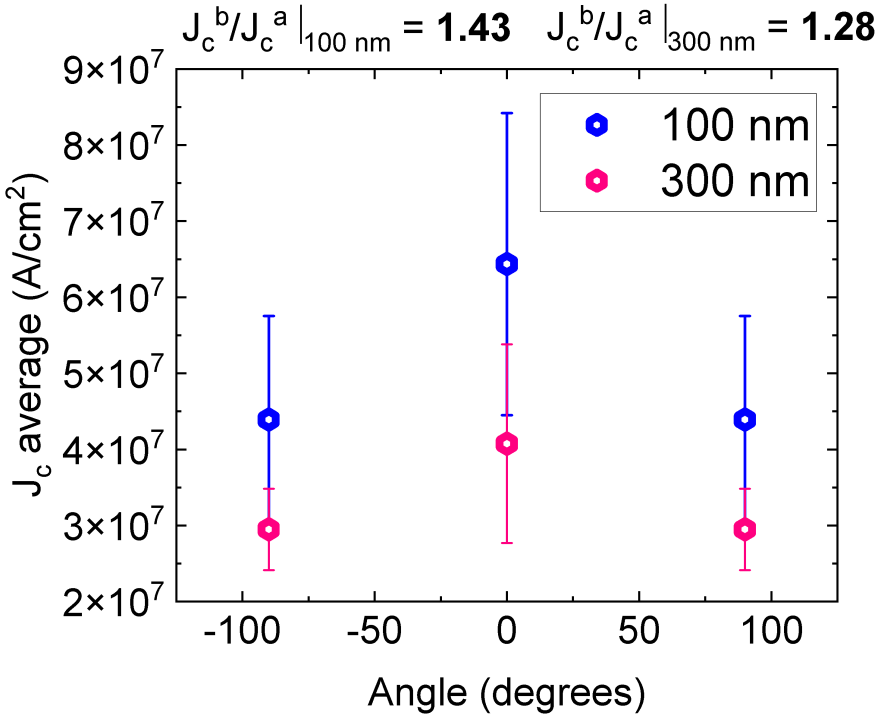

Figure 4.2: Average and standard deviation of the J_c distributions, for nanowires oriented either at 0 or at 90 degrees. Even though the error bars are quite large, we see a clear difference between the two directions, which points to a London anisotropy between the two in-plane directions. The J_c values measured in 300 nm wide wires are generally lower than in the case of narrower wires. This is due to current crowding effects, which are amplified by the width of the nanowires [51].

We observe that the J_c measured in the 100 nm wide wires are greater then the J_c measured in the wider ones. This can be explained taking into account current crowding effects at the extremities of the nanowires, which are greater for larger wires, and pushes the measured J_c further from the depairing current density limit.

The broadening of the distributions, i.e. the error bar, is rather large and it is width dependent, since it is almost a factor two larger for narrower wires: the understanding of the nature of these J_c fluctuations will be object of further studies, to understand if they are just extrinsic, and due to small differences between nominally identical nanowires, or directly related to the the intrinsic physics at play (nematicity).

However, as we can clearly see in figure 4.2, the measurement of a large population of identical wires overcomes any issues connected to these intrinsically large error bars: we can just consider the average and neglect the fluctuations of the J_c. Indeed, for both the populations, $w = 100$ nm and $w = 300$ nm, the averages are different at the two angles, with similar ratios. The London anisotrpy we found is aligned with what we would expect from the measurements of the external magnetic field periodicity of Dayem bridge YBCO nanoSQUIDs, according to which we have that $1 < \frac{\lambda_a}{\lambda_b} < 2$ [59]. which should stand out more in the case of thinner wires. In conclusion, a clear anisotropy of the critical density current along the two in-plane directions of the YBCO cell is present. This opens the way to our next experiment.

4.1.2. Angular dependence

The importance of the presence of the expected anisotropy contribution due to different λs along the two in-plane axis is twofold: on one side, we get the confirmation that intrinsic phenomena due to the structure of YBCO are preserved down to the nanoscale and can be studied in our nanowires; on the other side, the knowledge of the expected J_c anisotropy helps us to isolate and pick up the possible contribution of additional anisotropies, connected for instance to a superconducting nematic state.

After our preliminary test, we proceeded thence with the study of the full angular dependence of the J_c. We patterned nanowires along 36 different directions, ranging from 0 to 360 degrees, with a nanowire every 10 degrees. The wires were arranged in a sun-beam configuration, each of them extending radially from a common pad in the center of the cluster (see fig. 4.3).

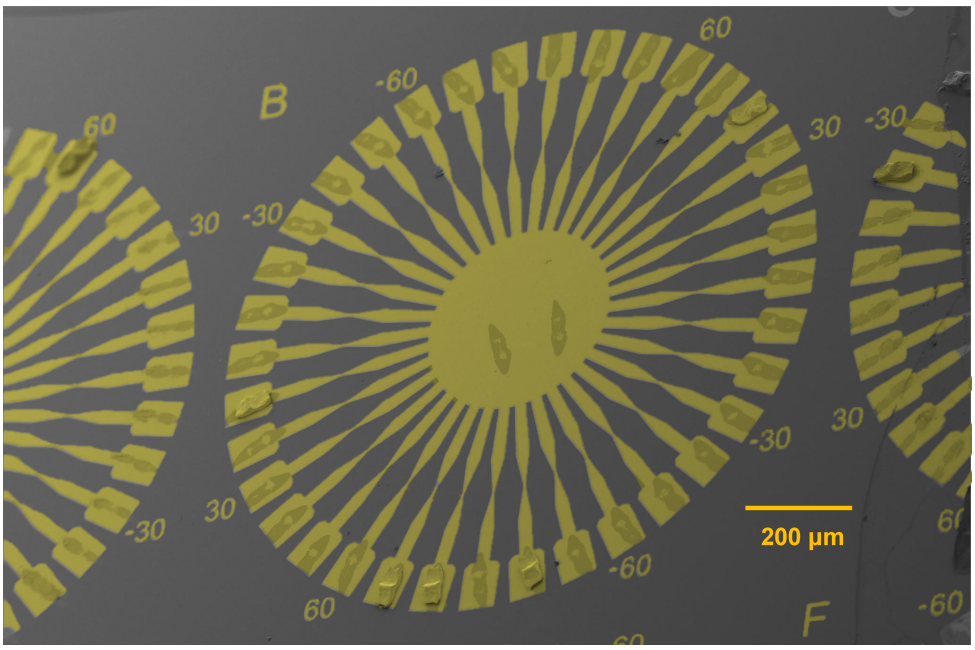

Figure 4.3: SEM picture of the nanowires arranged in a sunbeam configuration.

We fabricated a total of 9 sun-beams, all patterned on the same 30 nm thick YBCO film; in 5 of them we had 100 nm wide nanowires, in the remaining 4 we had instead the 300 nm wide ones. All measurements were performed in the same way as in the experiment discussed in the previous section.

Nematic order is supposed to break the four-fold rotational symmetry, but it still preserves 180° degrees symmetry (C2 point symmetry) and for this reason the relevant directions for every sun-beam were just half of the total, being the other half physically equivalent. Following the convention established before we plotted the data as a function of the angle, for values ranging from 90 to -90 degrees, with 0 degrees corresponding to the b-axis, 90 degrees to the a-axis and -90 simply being assigned the same data for the 90 degrees oriented wires. In Fig. 4.4(a) we have plotted all the J_cs collected during our measurements.

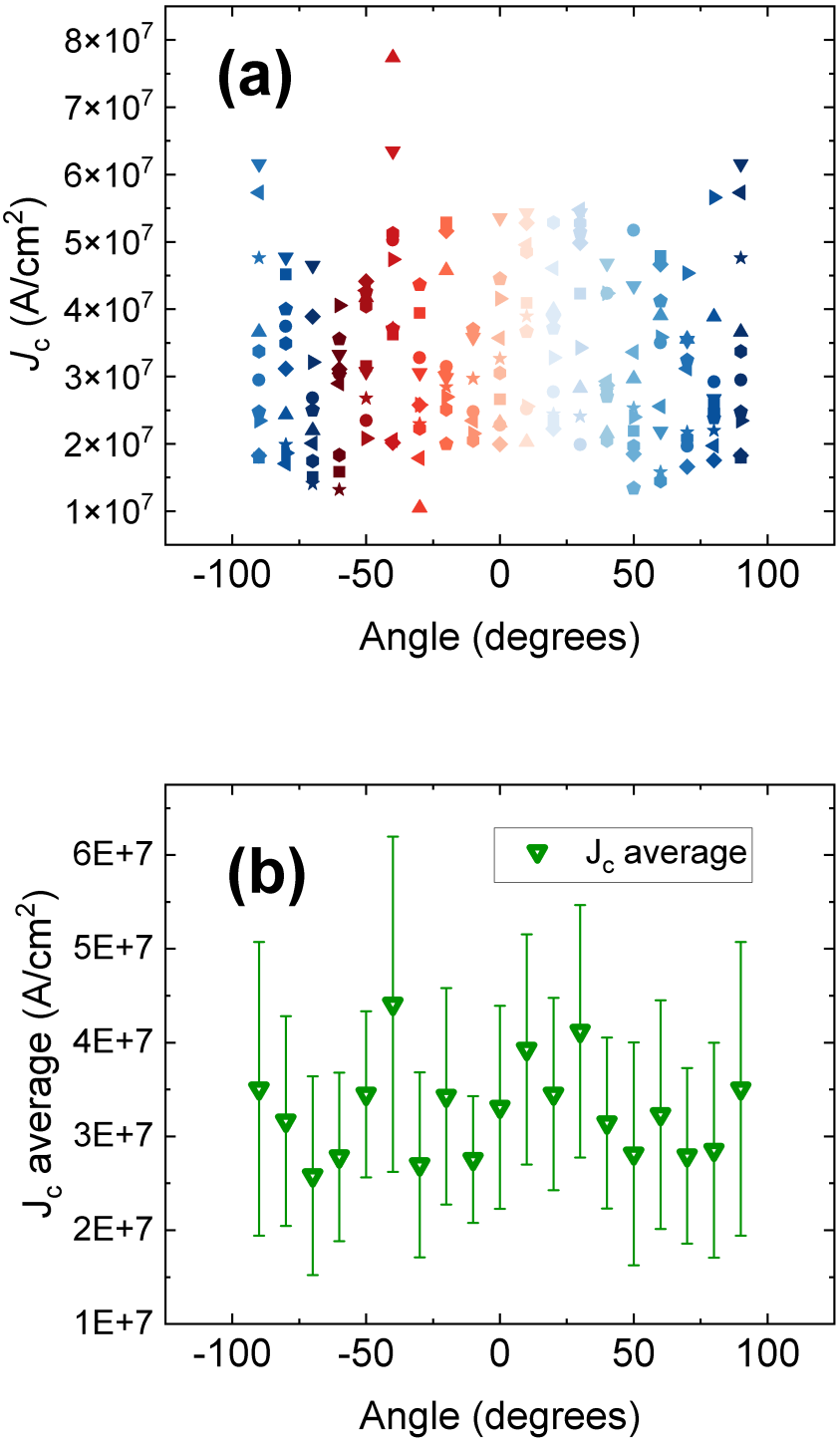

Figure 4.4: In panel (a) we have plotted the J_c that we have determined for every single measured nanowire. In panel (b) we have plotted the average of the J_c distribution for every angle, together with its broadening σ in the form of error bar.

Nominally there should be 8 values per angle in the case of the 300 nm wide wires and 10 values for the narrower wires. We could not measure every single wire but the percentage of non-functioning wires is nevertheless negligible. Starting from these data we evaluated the average and the broadening σ of the J_c distribution for every angle and we plotted these new values in Fig. 4.4(b).

In order to look for a possible nematic contribution, it is essential to remove from the data the anisotropy contribution to the J_c due to the different London penetration lengths along the two main axis, whose trend as a function of the angle γ is given by the following formula [60]:

$$J_c^{\lambda} = \sqrt{k_1 cos^2(\gamma) + k_2 sin^2(\gamma)} \tag{4.2}$$

The angle γ follows the same convention we established before and k_1 and k_2 are directly related to the two in-plane London penetration depths via the relation $\frac{k_1}{k_2} = \frac{\lambda_2}{\lambda_1}$.

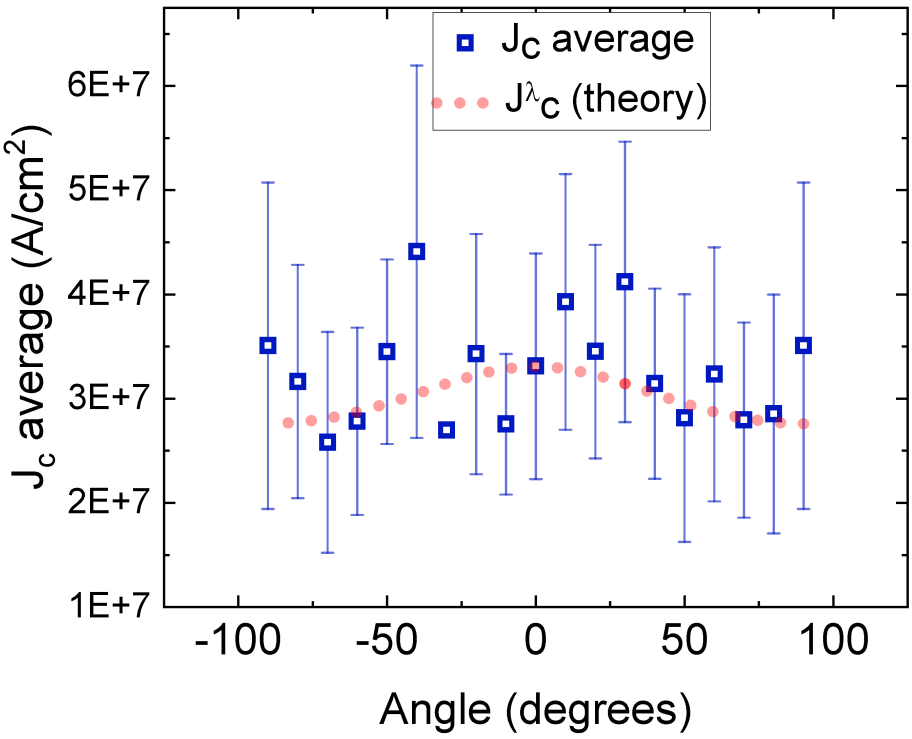

Figure 4.5: In this graph we highlighted with a red-dotted line the J_c contribution coming from the London anisotropy. To evaluate the k_1 and k_2 coefficients we used the J_c values we found in the previous experiment, where we measured only wires oriented along 0 and 90 degrees.

The values for k_1 and k_2 have been evaluated considering the data we got from the measurements discussed in the the previous section and this anisotropy contribution is plotted in the graph as a red-dotted-line.

In Fig. 4.6 we subtracted the London anisotropy component of the J_c and we observe a a modulation of the J_c. This modulation can be fitted by a sinusoidal curve (violet line).

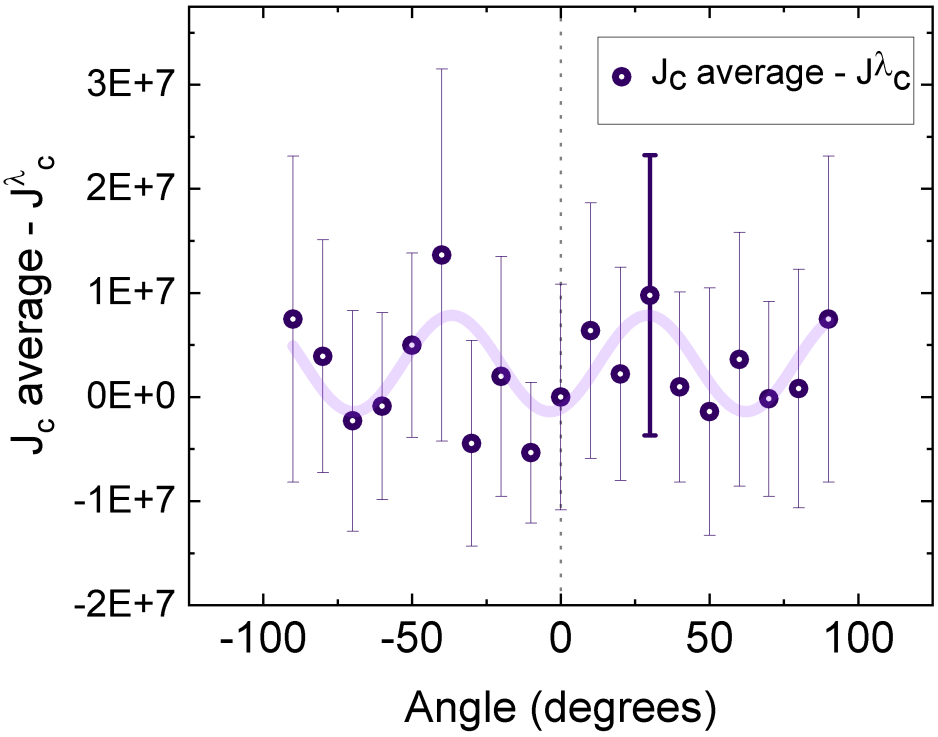

Figure 4.6: In this picture we removed the J_c contribution due to the London anisotropy and we fitted a sinusoidal curve on top of the data we obtained. As we can see, there is a modulation of the average values o the J_c, with a maximum in correspondence of 25°. The fact that the maxima of the modulation are not along the main crystallographic directions of the YBCO films might point to an anisotropy linked to a nematic behaviour.

From the sinusoidal fit, we have estimated a J_c maximum located around $\gamma = 25°$. If we associate this modulation to a nematic behaviour, this occurrence could be particularly interesting since it implies that the nematic anisotropy axis is not oriented along the main crystallographic axis.

Notably, the error bars are larger in correspondence of the maxima of the sinusoidal curve we fitted. Even though we cannot categorically exclude defects due to nanofabrication as

the origin of this occurrence, we tend to believe that this peculiar characteristic is related to the intrinsic physics of nematicity, according to which J_c fluctuations are higher when nematicity is stronger [61] [62]. Such origin would validate our fit on the averages, despite the whole modulation is well within the error bars.

5 | Confinement by thickness

In this chapter we will present the realization of underdoped a-axis oriented YBCO films and the results of their transport characterization. These films are particularly interesting, mainly for two reasons; first, the CuO_2 planes, where the different intertwined local orders of the underdoped regime reside, are perpendicular to the surface of the substrate and parallel to the growth direction. They are therefore constrained by the film thickness to form one-dimensional nanoribbons. Any nanofabrication procedure, which could potentially introduce unwanted defects into the final devices, is avoided.

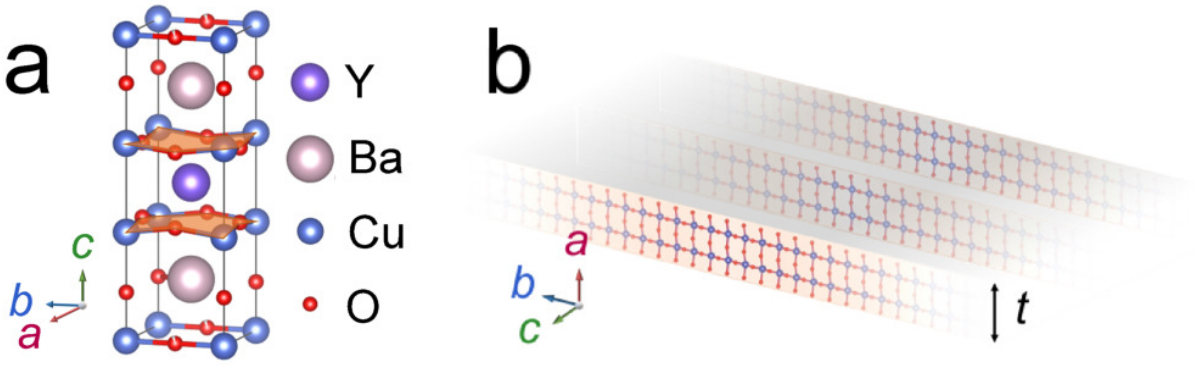

Figure 5.1: (a) Unit cell of YBCO. (b) Sketch of the structure of a-axis oriented films. The CuO_2 planes are perpendicular to the substrate and confined by the thickness of the film into nanobelts.

The second reason of interest resides in the possibity to study easily the electronic transport along the c-axis, which could be helpful in understanding the physics of YBCO.

By combining these two aspects, we could learn a lot from charge modulations, whose bulk form has a negligible correlation along the c-axis. The peculiar arrangement of the CuO_2 planes could set conditions on the CDW, allowing us to further explore this local order and get more insight in its intertwining with superconductivity.

5.1. Growth of underdoped a-axis oriented films

It is extremely important to get underdoped YBCO films, which can be then used to explore the underdoepd region of the the phase diagram, where all the local orders are located and many unusual phenomena that characterize cuprates are observed. The process needed to get high quality underdoped c-axis oriented YBCO films is well established [43, 63]: as we have discussed in chapter 2, by varying the post annealing pressure after the film deposition, one can get pristine YBCO samples with the desired doping level, characterized by a smooth and sharp superconducting transition.

However, the scenario for a-axis oriented YBCO is different. Oxygen inter-diffusion happens mostly along the a-b direction, where it is orders of magnitude higher than along the c-axis direction. So, a-axis oriented films have a completely different dynamics in the oxygenation, since we have a much larger area available for oxygen exchange. If we try the same process employed for c-axis films to get underdoped a-axis samples we get unsatisfactory results, with a $R(T)$ characterized by a broad and irregular superconducting transition and a supercondcting onset fixed at the optimally doped level, independently on the post-annealing pressure (see fig. 5.2(a)).

To overcome this problem, we developed a new technique to access the underdoped region [64], consisting in depositing a slightly overdoped sample and then reaching the desired doping by carrying out an $ex-situ$ annealing at a fixed and steady oxygen pressure. We observed that the films obtained with this technique show a good cristallinity and a smooth and sharp transition, sign of a better oxygenation of the sample (see fig. 5.2(b)).

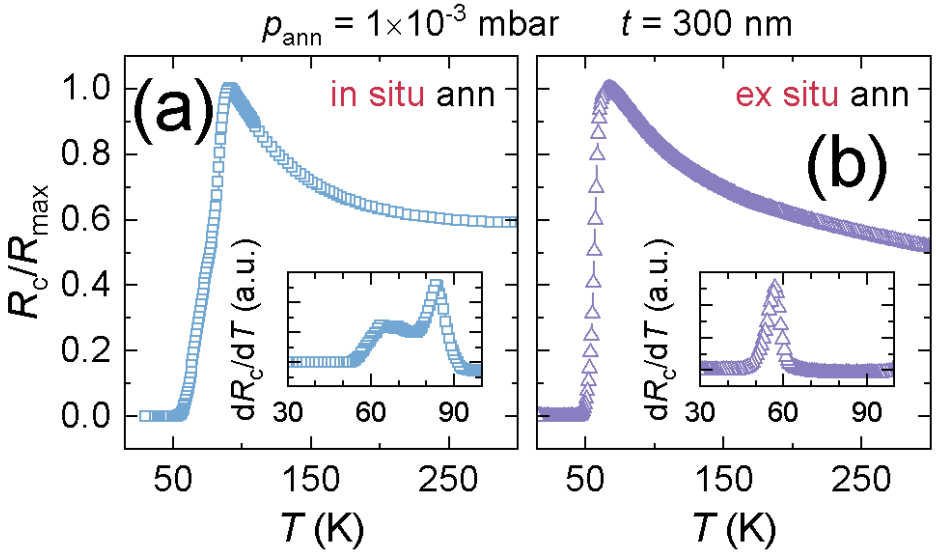

Figure 5.2: (a) R(T) curve of an underdoped *a*-axis oriented YBCO films obtained following the same procedure employed for *c*-axis oriented films; (b) R(T) curve of an underdoped *a*-axis oriented film obtained with the different procedure we described earlier in the text, consisting of an $ex - situ$ annealing starting from a slightly overdoped film. As we can see, in the former case we get an irregular (double) and broad superconducting transition, whereas in the latter we have a much better transition to a superconducting regime, sharper and smoother.

This new procedure offers the additional advantage to allow the modification of the doping of the same film several times. The whole underdoped side of the phase diagram can therefore be explored using a single sample, where only the oxygen content is modified.

Starting therefore from a 50 nm thick, slightly overdoped film, in the experiment here presented we have explored the whole phase diagram: we decreased each time the annealing oxygen pressure, performing X-Ray diffraction (XRD) measurements and $R(T)$ measurement after each annealing.

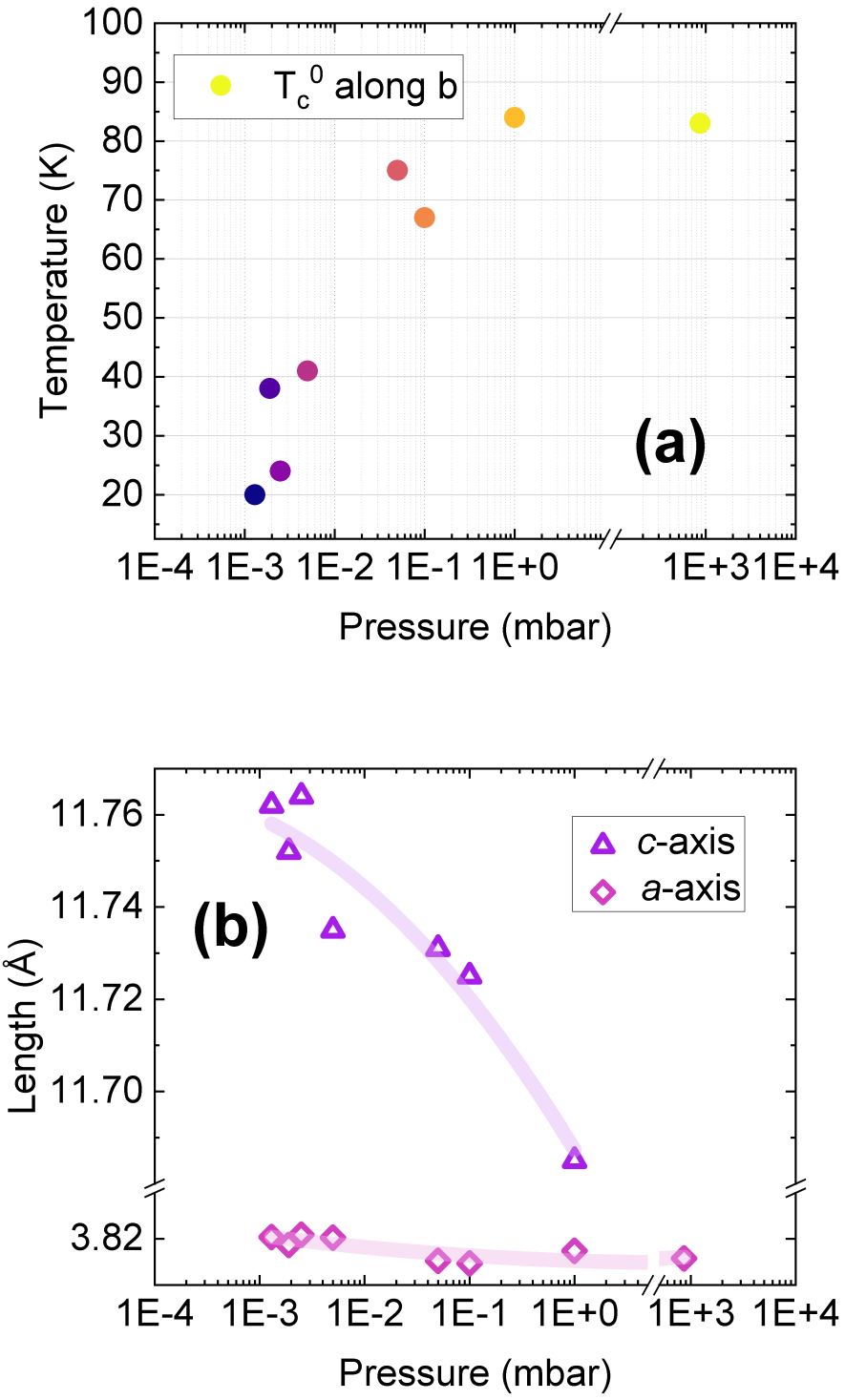

Figure 5.3: (a) T_c^0 along the b-axis versus the pressure employed during the annealing process. We obtained a T_c^0 which is generally decreasing, sign of films becoming more and more underdoped. This is further confirmed by XRD measurements in panel (b), which show a c-axis getting longer, proof that we are actually subtracting oxygen from the chains and getting to the underdoped region of the phase diagram. We also observe, as we would expect, an increase of the a-axis.

The X-Ray Diffraction analysis has been employed to determine the twinning state (the films are totally detwinned) and the length of the a and c axis, starting from the position of their peaks in the two configuration of measurements we have discussed in chapter 2. The data show an increase of both c and a axis, as one would expect when going to the underdoped, where the oxygen chains along the b-axis become less populated causing the other two axis to increase in length. This increase and the good crystalline quality observed each time in the symmetric $2\theta - \omega$ scans confirm the validity of the method we employed to achieve underdoped films.

5.2. Transport anomalies in ultrathin and underdoped a-axis oriented films

In plane transport measurements were performed on the same 50 nm thick film during all the experiment, after each annealing. We measured the in plane resistance vs temperature along the two main directions, using a four-contact Van der Pauw configuration [40]. All the data we collected are plotted in the two graphs below. The curves refer to different dopings (on the underdoped side of the phase diagram) and are characterized by rather sharp superconducting transition; nevertheless already from a first look the $R(T)$ curves are characterized by peculiar features that differentiate them from the resistance behaviour we observe in the bulk.

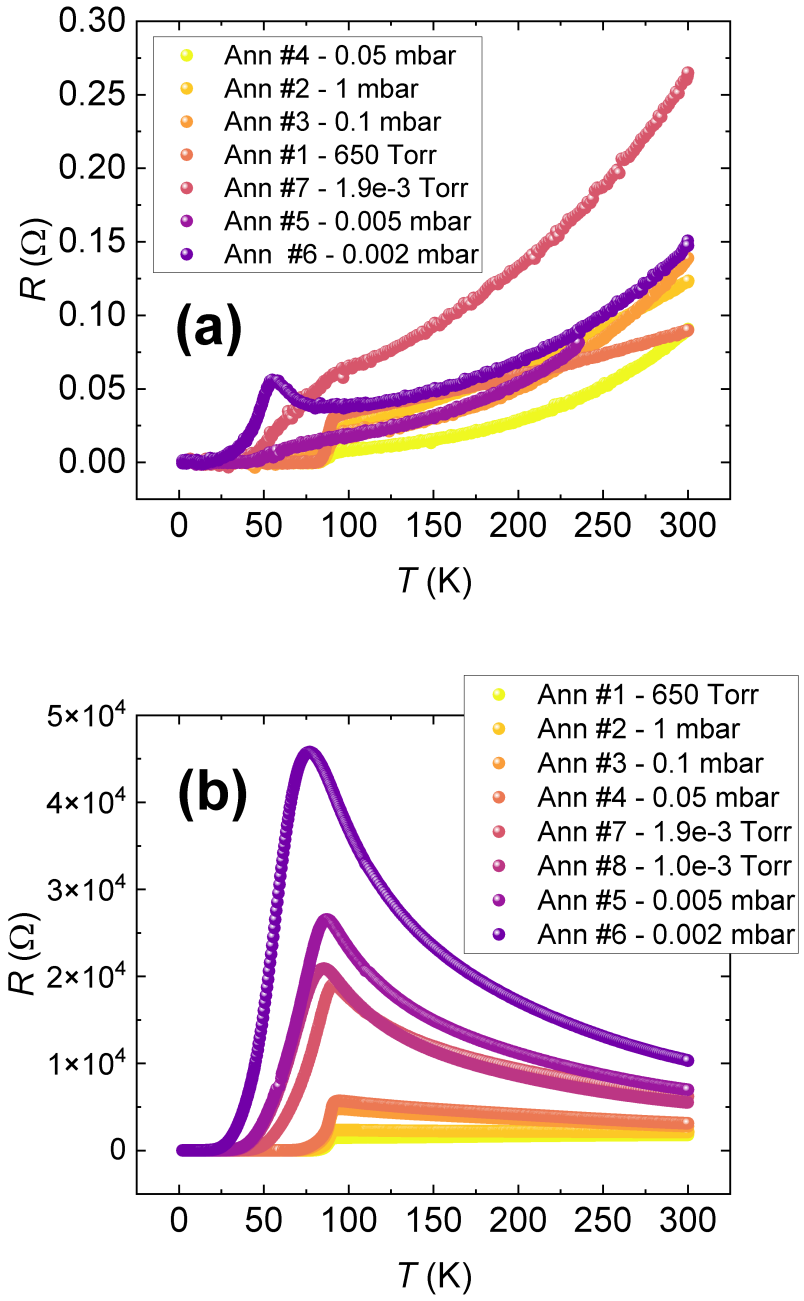

Figure 5.4: (a) $R(T)$ measured along the b-axis on the same film annealed at different pressures. Interestingly, we observe an upturn in the resistance at the lowest doping we were able to reach. (b) Same as panel a, but the measurements are here along the c-axis direction.

Figure 5.2(a) shows how in the case of the $R(T)$ along the b axis we can observe the total disappearance of the linear-in-T resistance, signature of the strange metal phase. If we make a comparison (see Fig. 5.5(a) and (b)) between the $R(T)$ measured on two different

YBCO samples at the same doping level (p=0.14), one c-axis oriented and the other a-axis oriented, we observe a radically different trend of the resistance at high temperatures. The b-axis resistance measured from the c-axis oriented sample shows a clear linear behaviour at high temperatures as one would expect from the presence of the strange metal phase which emerges out of the pseudogap regime. In the case of the a-axis oriented YBCO film, we have instead a resistance which follows a clear metallic-like parabolic trend, typical of a Fermi liquid (see pic. 5.5). The reason for that could be due to a strong role played by the chains, which are oriented along the b-axis direction. In such constrained films they might be - with respect to isodoped c-axis oriented films - very ordered and coherent among each other, pervasively influencing the transport in the normal state.

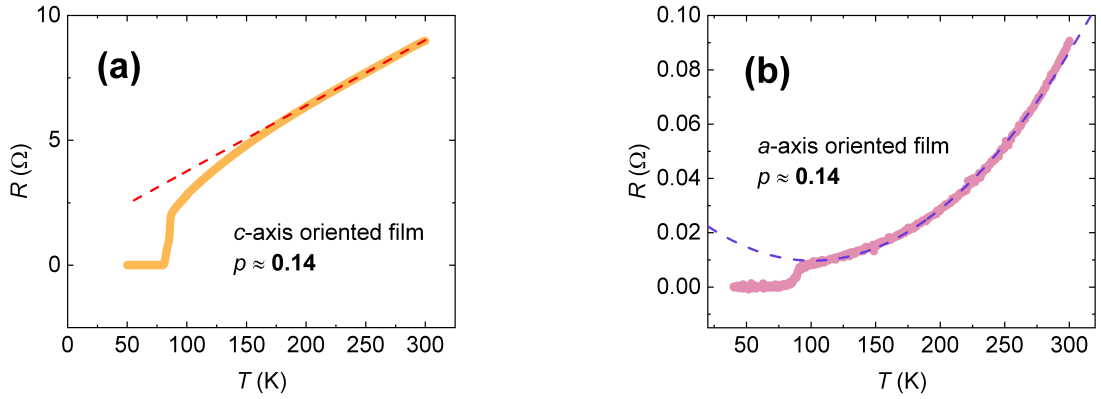

Figure 5.5: Here we have a comparison between two $R(T)$ curves coming from two different underdoped YBCO films. Picture (a) shows the resistance along the b-axis in the case of a c-axis oriented film; at high temperature we see the conventional linear behaviour of the resistivity due to the strange metal regime, which emerges out of the pseudogap, where we can instead observe a parabolic trend of the resistance. Picture (b) shows instead a the resistance along the b-axis in the case of a a-axis oriented film; notably, the resistance follows a clear metallic quadratic behaviour, in full agreement with the Fermi-liquid theory.

The second notable feature emerging from the transport measurements is the huge anisotropy between the resistance measured along the b-axis and the one along the c-axis, whose ratio can reach the order of 10^6 (see pic. 5.6).

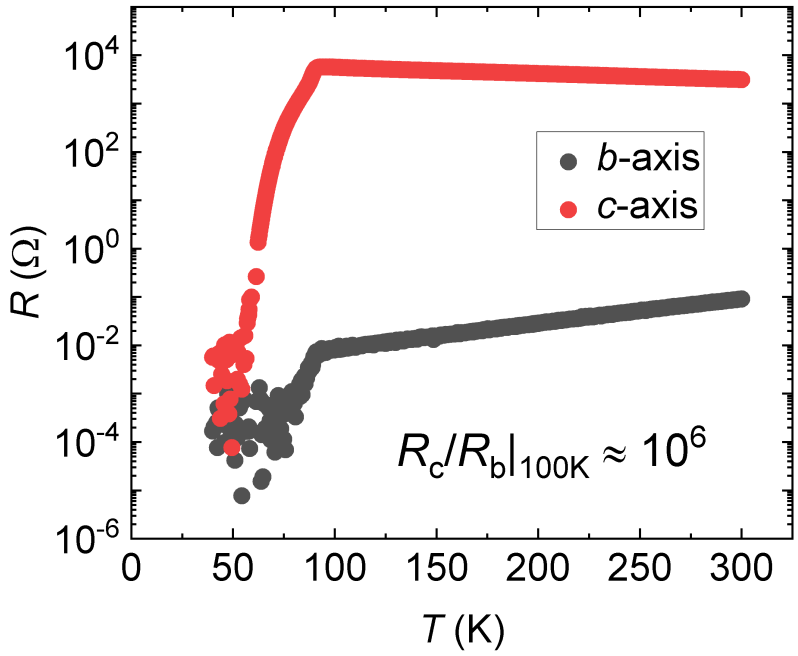

Figure 5.6: In the picture we have plotted in logarithmic scale the resistance measured along both b-axis and c-axis at the same doping level (p=0.14). The anisotropy, which reaches values on the order of 10^6, is greater at 100 K due to the peculiar behaviour of the resistance along the c-axis, which shows an insulating-like growth until the superconducting transition is reached.

Such high anisotropy values have been observed both in LaSCO and BiSCCO, where there is a much smaller coupling between the CuO_2 planes due to their higher distance. This suggests that the weak coupling between adjacent CuO_2 planes in a-axis films, highlighted by the insulator-like temperature dependence of R_c, is modified as an effect of the confinement, and is possibly made even weaker.

6 | Conclusions and future developments

We presented the results of our measurements on two radically different kinds of YBCO samples, which have in common the confinement of the CuO_2 planes. The goal of the experiments was to exploit this confinement to get an insight on the nanoscale orders that characterize and seem to govern the transport properties of cuprate superconductors.

The first samples we have investigated were *c*-axis oriented slightly overdoped YBCO thin films, where the confinement has been realized through nanopatterning of the material, squeezing therefore YBCO into nanowires, with cross section down to 30x100 nm^2. We have patterned these nanowires as a function of the in-plane angle, to check how the critical current density J_c evolves as a function of the angle. We have observed that, on top of the expected J_c anisotropy due to the orthorhombic structure, therefore to the anisotropic London penetration depths along the a and b axis directions, an additional anisotropy is present. Indeed, we have observed a sinusoidal modulation of the J_c with the angle, not aligned with the crystallographic axis, which might be a signature of a nematic order in the superconducting state, i.e. of a nematic condensate of cooper pairs. The fluctuations of the J_c are large, with the error bars wider than the amplitude of the sinusoidal curve we fitted; nevertheless the fluctuations are higher when nematicity appears to be stronger, in agreement with recent theories predicting this phenomenon in terms of nematicity itself. Our data cannot exclude categorically the influence of extrinsic factors on the large fluctuations. To better elucidate on this issue, a possible strategy to be tried in the next future could be the following: first, one could increase the statistics to increase the reliability of the data, measuring more nanowires; second, a thorough SEM investigation could be carried out on the wires, in order to look for defects and/or to measure the actual widths, which might differ from the nominal ones: in both cases, this would possibly lead to a reduction of the high fluctuations of J_c in the measured distributions.

The second samples we have investigated were *a*-axis oriented YBCO thin films, where the

confinement is a mere consequence of the thickness of the films, transforming the CuO_2 planes into nanoribbons. First task we accomplished was the growth of underdoped and untwinned YBCO thin films, where we took advantage of an $ex-situ$ oxygen annealing procedure. This procedure also offered to us the additional advantage to span the whole underdoped side of the phase diagram using a single film: this allowed us to investigate the different intertwined orders populating the underdoped region of the phase diagram by using the same platform, where only the oxygen content is modified but all the other material properties are unchanged. The $R(T)$ measurements we carried out on the CuO_2 nanoribbons showed two surprising features: i) a full parabolic behaviour of the resistance at high temperatures and ii) high anisotropy of the resistance measured along the two in-plane axis b and c. The high anisotropy could be due to the low coupling between the CuO_2 planes, which gets even weaker confining them at the nanoscale. Cuprates superconductivity lies entirely in the CuO_2 planes, but this very weak coupling we observe, which produces a resistance anisotropy comparable to the one of 2D materials like BiSCCO and LaSCO, could introduce some constraints on the superconducting carriers wave-functions. If we take this almost complete decoupling into account we have then well-defined boundary conditions along the c-axis, which would lead to a modification of the transport along the perpendicular direction, the b-axis, in which we observed the complete disappearance of the strange metal state and a full restoration of the Fermi liquid behaviour. This feature of the transport along b deserves further investigation: we believe it might be due to the CuO chains, which - confined at the nonoscale - present a level of order and coherence much greater than in the c-axis oriented films. One of the possible approaches for future research would be repeating the same measurements on films of different thicknesses to better study the influence of strain, which has been proven multiple times to be a key factor in shaping the physics of cuprates superconductors. If the Fermi liquid-like resistance would be confirmed this could open the doors to a better understanding of the oxygen-chains and the role of transport in the CuO_2 planes, which could be fundamental in solving the grand-challenge of superconductivity in cuprates. Another possible way to take advantage of this peculiar arrangement of the CuO_2 planes could be to study how the charge order is influenced by their confinement. As mentioned in the first chapter, CDW are a biaxial excitation, happening mainly in the $a-b$ planes. Being these planes arranged perpendicularly to the substrate in the form of nanoribbons, one could have plenty of room to investigate charge modulations along the c-axis, to possibly get a clearer picture of the electronic coupling between CuO_2 planes. Furthermore, the structure which characterizes a-axis oriented films could introduce constraints in the charge modulations, locking their frequency of oscillation to a discrete range of values. Once again, this kind of experiments could help us to shed light on the physics of these

fascinating materials and the orders that define them, allowing us to find a solution to the mystery of the high-T_c superconductivity.

Bibliography

[1] W. Meissner and R. Ochsenfeld, "Ein neuer effekt bei eintritt der supraleitfähigkeit," *Naturwissenschaften*, vol. 21, no. 44, pp. 787–788, 1933.

[2] F. London and H. London, "The electromagnetic equations of the supraconductor," *Proceedings of the Royal Society of London. Series A-Mathematical and Physical Sciences*, vol. 149, no. 866, pp. 71–88, 1935.

[3] V. L. Ginzburg and L. D. Landau, "On the theory of superconductivity," in *On superconductivity and superfluidity*, pp. 113–137, 2009.

[4] E. Maxwell, "Isotope effect in the superconductivity of mercury," *Phys. Rev.*, vol. 78, no. 4, p. 477, 1950.

[5] J. Bardeen, L. N. Cooper, and J. R. Schrieffer, "Theory of superconductivity," *Phys. Rev.*, vol. 108, no. 5, p. 1175, 1957.

[6] B. Keimer, S. A. Kivelson, M. R. Norman, S. Uchida, and J. Zaanen, "From quantum matter to high-temperature superconductivity in copper oxides," *Nature*, vol. 518, no. 7538, pp. 179–186, 2015.

[7] E. Wahlberg, *Reshaping the Phase Diagram of $YBa_2Cu_3O_{7-\delta}$ Through Strain in Ultrathin Films and Nanowires*. 2021.

[8] C. Villard, G. Koren, D. Cohen, E. Polturak, B. Thrane, and D. Chateignier, "*ab*-plane anisotropy of transport properties in unidirectionally twinned $YBa_2Cu_3O_{7-\delta}$ films," *Phys. Rev. Lett.*, vol. 77, no. 18, p. 3913, 1996.

[9] H. Smilde, A. A. Golubov, G. Rijnders, J. Dekkers, S. Harkema, D. Blank, H. Rogalla, H. Hilgenkamp, *et al.*, "Admixtures to $d-wave$ gap symmetry in untwinned $YBa_2Cu_3O_{7-\delta}$ superconducting films measured by angle-resolved electron tunneling," *Phys. Rev. Lett.*, vol. 95, no. 25, p. 257001, 2005.

[10] S. Johnson, E. Forgan, S. Lloyd, C. Aegerter, S. Lee, R. Cubitt, P. Kealey, C. Ager, S. Tajima, A. Rykov, *et al.*, "Flux-line lattice structures in untwinned $YBa_2Cu_3O_{7-\delta}$," *Phys. Rev. Lett.*, vol. 82, no. 13, p. 2792, 1999.

[11] D. Lu, D. Feng, N. Armitage, K. Shen, A. Damascelli, C. Kim, F. Ronning, Z.-X. Shen, D. Bonn, R. Liang, *et al.*, "Superconducting gap and strong in-plane anisotropy in untwinned $YBa_2Cu_3O_{7-\delta}$," *Phys. Rev. Lett.*, vol. 86, no. 19, p. 4370, 2001.

[12] T. Sekitani, N. Miura, S. Ikeda, Y. Matsuda, and Y. Shiohara, "Upper critical field for optimally-doped $YBa_2Cu_3O_{7-\delta}$," *Phys. B: Condens. Matter*, vol. 346, pp. 319–324, 2004.

[13] D. Gustafsson, D. Golubev, M. Fogelström, T. Claeson, S. Kubatkin, T. Bauch, and F. Lombardi, "Fully gapped superconductivity in a nanometre-size a method of measuring specific resistivity and hall effect of discs of arbitrary shape island enhanced by a magnetic field," *Nat. Nanotechno.*, vol. 8, no. 1, pp. 25–30, 2013.

[14] D. J. Van Harlingen, "Phase-sensitive tests of the symmetry of the pairing state in the high-temperature superconductors—evidence for $d_{x^2+y^2}$ symmetry," *Rev. of Mod. Phys.*, vol. 67, no. 2, p. 515, 1995.

[15] J. Zaanen and O. Gunnarsson, "Charged magnetic domain lines and the magnetism of high-T_c oxides," *Phys. Rev. B*, vol. 40, no. 10, p. 7391, 1989.

[16] K. Machida, "Magnetism in La_2CuO_4 based compounds," *Phys. C: Supercond.*, vol. 158, no. 1-2, pp. 192–196, 1989.

[17] J. Tranquada, B. Sternlieb, J. Axe, Y. Nakamura, and S.-i. Uchida, "Evidence for stripe correlations of spins and holes in copper oxide superconductors," *Nature*, vol. 375, no. 6532, pp. 561–563, 1995.

[18] G. Ghiringhelli, M. Le Tacon, M. Minola, S. Blanco-Canosa, C. Mazzoli, N. Brookes, G. De Luca, A. Frano, D. Hawthorn, F. He, *et al.*, "Long-range incommensurate charge fluctuations in (Y, Nd) $Ba_2Cu_2O_{6+\delta}$," *Science*, vol. 337, no. 6096, pp. 821–825, 2012.

[19] P. Monceau, "Electronic crystals: an experimental overview," *Adv. Phys.*, vol. 61, no. 4, pp. 325–581, 2012.

[20] T. Wu, H. Mayaffre, S. Krämer, M. Horvatić, C. Berthier, W. Hardy, R. Liang, D. Bonn, and M.-H. Julien, "Incipient charge order observed by NMR in the normal state of $YBa_2Cu_3O_{7-\delta}$," *Nat. Commun.*, vol. 6, no. 1, p. 6438, 2015.

[21] J. Chang, E. Blackburn, O. Ivashko, A. Holmes, N. B. Christensen, M. Hücker, R. Liang, D. Bonn, W. Hardy, U. Rütt, *et al.*, "Magnetic field controlled charge density wave coupling in underdoped $YBa_2Cu_3O_{6+\delta}$," *Nat. Commun.*, vol. 7, no. 1, p. 11494, 2016.

[22] S. Blanco-Canosa, A. Frano, E. Schierle, J. Porras, T. Loew, M. Minola, M. Bluschke, E. Weschke, B. Keimer, and M. Le Tacon, "Resonant x-ray scattering study of charge-density wave correlations in $YBa_2Cu_3O_{6+\delta}$," *Phys. Rev. B*, vol. 90, no. 5, p. 054513, 2014.

[23] J. Chang, E. Blackburn, A. Holmes, N. B. Christensen, J. Larsen, J. Mesot, R. Liang, D. Bonn, W. Hardy, A. Watenphul, *et al.*, "Direct observation of competition between superconductivity and charge density wave order in $YBa_2Cu_3O_{7-\delta}$," *Nat. Phys.*, vol. 8, no. 12, pp. 871–876, 2012.

[24] Y. Ando, S. Komiya, K. Segawa, S. Ono, and Y. Kurita, "Electronic phase diagram of high-T_c cuprate superconductors from a mapping of the in-plane resistivity curvature," *Phys. Rev. Lett.*, vol. 93, no. 26, p. 267001, 2004.

[25] R. Liang, D. Bonn, and W. Hardy, "Evaluation of CuO_2 plane hole doping in $YBa_2Cu_3O_{7-\delta}$ single crystals," *Phys. Rev. B*, vol. 73, no. 18, p. 180505, 2006.

[26] M. E. Barber, H.-h. Kim, T. Loew, M. L. Tacon, M. Minola, M. Konczykowski, B. Keimer, A. P. Mackenzie, and C. W. Hicks, "Suppression of superconductivity by charge density wave order in $YBa_2Cu_3O_{7-\delta}$," *arXiv preprint arXiv:2101.02923*, 2021.

[27] R. Arpaia, S. Caprara, R. Fumagalli, G. De Vecchi, Y. Peng, E. Andersson, D. Betto, G. De Luca, N. Brookes, F. Lombardi, *et al.*, "Dynamical charge density fluctuations pervading the phase diagram of a cu-based high-T_c superconductor," *Science*, vol. 365, no. 6456, pp. 906–910, 2019.

[28] R. Arpaia and G. Ghiringhelli, "Charge order at high temperature in cuprate superconductors," *J. Phys. Soc. Jpn*, vol. 90, no. 11, p. 111005, 2021.

[29] S. Nakata, M. Horio, K. Koshiishi, K. Hagiwara, C. Lin, M. Suzuki, S. Ideta, K. Tanaka, D. Song, Y. Yoshida, *et al.*, "Nematicity in a cuprate superconductor revealed by angle-resolved photoemission spectroscopy under uniaxial strain," *npj Quantum Mater.*, vol. 6, no. 1, p. 86, 2021.

[30] O. Cyr-Choinière, G. Grissonnanche, S. Badoux, J. Day, D. Bonn, W. Hardy, R. Liang, N. Doiron-Leyraud, and L. Taillefer, "Two types of nematicity in the phase diagram of the cuprate superconductor $YBa_2Cu_3O_{7-\delta}$," *Phys. Rev. B*, vol. 92, no. 22, p. 224502, 2015.

[31] H. Murayama, Y. Sato, R. Kurihara, S. Kasahara, Y. Mizukami, Y. Kasahara, H. Uchiyama, A. Yamamoto, E.-G. Moon, J. Cai, *et al.*, "Diagonal nematicity in the pseudogap phase of $HgBa_2CuO_{4+\delta}$," *Nat. Commun.*, vol. 10, no. 1, p. 3282, 2019.

[32] J. Wu, A. Bollinger, X. He, and I. Božović, "Spontaneous breaking of rotational symmetry in copper oxide superconductors," *Nature*, vol. 547, no. 7664, pp. 432–435, 2017.

[33] Y. Cao, D. Rodan-Legrain, J. M. Park, N. F. Yuan, K. Watanabe, T. Taniguchi, R. M. Fernandes, L. Fu, and P. Jarillo-Herrero, "Nematicity and competing orders in superconducting magic-angle graphene," *Science*, vol. 372, no. 6539, pp. 264–271, 2021.

[34] L. Nie, K. Sun, W. Ma, D. Song, L. Zheng, Z. Liang, P. Wu, F. Yu, J. Li, M. Shan, *et al.*, "Charge-density-wave-driven electronic nematicity in a kagome superconductor," *Nature*, vol. 604, no. 7904, pp. 59–64, 2022.

[35] S. Lederer, Y. Schattner, E. Berg, and S. A. Kivelson, "Enhancement of superconductivity near a nematic quantum critical point," *Phys. Rev. Lett.*, vol. 114, no. 9, p. 097001, 2015.

[36] S. Hosoi, K. Matsuura, K. Ishida, H. Wang, Y. Mizukami, T. Watashige, S. Kasahara, Y. Matsuda, and T. Shibauchi, "Nematic quantum critical point without magnetism in $FeSe_{1-\delta}S_{\delta}$ superconductors," *Proc. Natl. Acad. Sci. U.S.A.*, vol. 113, no. 29, pp. 8139–8143, 2016.

[37] E. Wahlberg, R. Arpaia, G. Seibold, M. Rossi, R. Fumagalli, E. Trabaldo, N. B. Brookes, L. Braicovich, S. Caprara, U. Gran, *et al.*, "Restored strange metal phase through suppression of charge density waves in underdoped $YBa_2Cu_3O_{7-\delta}$," *Science*, vol. 373, no. 6562, pp. 1506–1510, 2021.

[38] T. J. Roskamp, "Exploring underdoped $YBa_2Cu_3O_{7-\delta}$: nanofabrication, thermomigration and pair-density waves," 2022.

[39] R. Arpaia, E. Andersson, A. Kalaboukhov, E. Schröder, E. Trabaldo, R. Ciancio, G. Dražić, P. Orgiani, T. Bauch, and F. Lombardi, "Untwinned $YBa_2Cu_3O_{7-\delta}$ thin films on MgO substrates: A platform to study strain effects on the local orders in cuprates," *Phys. Rev. Mater.*, vol. 3, no. 11, p. 114804, 2019.

[40] O. Philips' Gloeilampenfabrieken, "A method of measuring specific resistivity and Hall effect of discs of arbitrary shape," *Philips Res. Rep.*, vol. 13, no. 1, p. 334, 1958.

[41] R. Baghdadi, R. Arpaia, T. Bauch, and F. Lombardi, "Toward $YBa_2Cu_3O_{7-\delta}$ nanoscale structures for hybrid devices," *IEEE Trans. Appl. Supercond.*, vol. 25, p. 1100104, 2015.

[42] R. Arpaia, D. Golubev, R. Baghdadi, R. Ciancio, G. Dražić, P. Orgiani, D. Monte-

murro, T. Bauch, and F. Lombardi, "Transport properties of ultrathin $YBa_2Cu_3O_{7-\delta}$ nanowires: A route to single-photon detection," *Phys. Rev. B*, vol. 96, no. 6, p. 064525, 2017.

[43] R. Arpaia, E. Andersson, E. Trabaldo, T. Bauch, and F. Lombardi, "Probing the phase diagram of cuprates with $YBa_2Cu_3O_{7-\delta}$ thin films and nanowires," *Phys. Rev. Mater.*, vol. 2, no. 2, p. 024804, 2018.

[44] R. Baghdadi, R. Arpaia, E. Stepantsov, M. Arzeo, D. Golubev, D. Montemurro, E. Andersson, T. Bauch, and F. Lombardi, "Study of in-plane electrical transport anisotropy of *a*-axis oriented $YBa_2Cu_3O_{7-\delta}$ nanodevices," *Phys. Rev. B*, vol. 95, no. 18, p. 184505, 2017.

[45] J. Bonetti, D. Caplan, D. Van Harlingen, and M. Weissman, "Electronic transport in underdoped $YBa_2Cu_3O_{7-\delta}$ nanowires: Evidence for fluctuating domain structures," *Phys. Rev. Lett.*, vol. 93, no. 8, p. 087002, 2004.

[46] G. Papari, F. Carillo, D. Stornaiuolo, L. Longobardi, F. Beltram, and F. Tafuri, "High critical current density and scaling of phase-slip processes in YBCO nanowires," *Supercond. Sci. Technol.*, vol. 25, no. 3, p. 035011, 2012.

[47] P. Larsson, B. Nilsson, and Z. Ivanov, "Fabrication and transport measurements of $YBa_2Cu_3O_{7-\delta}$ nanostructures," *J. Vac. Sci. Technol.*, vol. 18, no. 1, pp. 25–31, 2000.

[48] J. Schneider, H. Kohlstedt, and R. Wördenweber, "Nanobridges of optimized $YBa_2Cu_3O_{7-\delta}$ thin films for superconducting flux-flow type devices," *Appl. Phys. Lett.*, vol. 63, no. 17, pp. 2426–2428, 1993.

[49] S. Nawaz, R. Arpaia, T. Bauch, and F. Lombardi, "Approaching the theoretical depairing current in $YBa_2Cu_3O_{7-\delta}$ nanowires," *Physica C*, vol. 495, pp. 33–38, 2013.

[50] R. Arpaia, S. Nawaz, F. Lombardi, and T. Bauch, "Improved nanopatterning for YBCO nanowires approaching the depairing current," *IEEE Trans. Appl. Supercond.*, vol. 23, no. 3, pp. 1101505–1101505, 2013.

[51] S. Nawaz, R. Arpaia, F. Lombardi, and T. Bauch, "Microwave response of superconducting $YBa_2Cu_3O_{7-\delta}$ nanowire bridges sustaining the critical depairing current: Evidence of josephson-like behavior," *Phys. Rev. Lett.*, vol. 110, no. 16, p. 167004, 2013.

[52] R. Baghdadi, R. Arpaia, S. Charpentier, D. Golubev, T. Bauch, and F. Lombardi, "Fabricating nanogaps in $YBa_2Cu_3O_{7-\delta}$ for hybrid proximity-based josephson junctions," *Phys. Rev. Appl.*, vol. 4, no. 1, p. 014022, 2015.

[53] S. Charpentier, R. Arpaia, J. Gaudet, D. Matte, R. Baghdadi, T. Löfwander, D. Golubev, P. Fournier, T. Bauch, and F. Lombardi, "Hot spot formation in electron-doped PCCO nanobridges," *Phys. Rev. B*, vol. 94, no. 6, p. 060503, 2016.

[54] R. Arpaia, D. Golubev, R. Baghdadi, M. Arzeo, G. Kunakova, S. Charpentier, S. Nawaz, F. Lombardi, and T. Bauch, "Resistive state triggered by vortex entry in $YBa_2Cu_3O_{7-\delta}$ nanostructures," *Physica C*, vol. 506, pp. 165–168, 2014.

[55] R. Arpaia, M. Ejrnaes, L. Parlato, F. Tafuri, R. Cristiano, D. Golubev, R. Sobolewski, T. Bauch, F. Lombardi, and G. Pepe, "High-temperature superconducting nanowires for photon detection," *Physica C*, vol. 509, pp. 16–21, 2015.

[56] M. Ejrnaes, L. Parlato, R. Arpaia, T. Bauch, F. Lombardi, R. Cristiano, F. Tafuri, and G. Pepe, "Observation of dark pulses in 10 nm thick YBCO nanostrips presenting hysteretic current voltage characteristics," *Supercond. Sci. Technol.*, vol. 30, no. 12, p. 12LT02, 2017.

[57] M. Arzeo, R. Arpaia, R. Baghdadi, F. Lombardi, and T. Bauch, "Toward ultra high magnetic field sensitivity $YBa_2Cu_3O_{7-\delta}$ nanowire based superconducting quantum interference devices," *J. Appl. Phys.*, vol. 119, no. 17, p. 174501, 2016.

[58] E. Trabaldo, R. Arpaia, M. Arzeo, E. Andersson, D. Golubev, F. Lombardi, and T. Bauch, "Transport and noise properties of YBCO nanowire based nanosquids," *Supercond. Sci. Technol.*, vol. 32, no. 7, p. 073001, 2019.

[59] R. Arpaia, *$YBa_2Cu_3O_{7-\delta}$ Nanowires to Study Nanoscale Ordering in High-T_c Superconductors*. Chalmers Tekniska Hogskola (Sweden), 2016.

[60] J. Johansson, K. Cedergren, T. Bauch, and F. Lombardi, "Properties of inductance and magnetic penetration depth in (103)-oriented $YBa_2Cu_3O_{7-\delta}$ thin films," *Phys. Rev. B*, vol. 79, no. 21, p. 214513, 2009.

[61] J. Wårdh and M. Granath, "Nematic single-component superconductivity and loop-current order from pair-density wave instability," *arXiv preprint arXiv:2203.08250*, 2022.

[62] J. Wårdh, M. Granath, J. Wu, A. Bollinger, X. He, and I. Božović, "Colossal transverse magnetoresistance due to nematic superconducting phase fluctuations in a copper oxide," *arXiv preprint arXiv:2203.06769*, 2022.

[63] E. Andersson, R. Arpaia, E. Trabaldo, T. Bauch, and F. Lombardi, "Fabrication and electrical transport characterization of high quality underdoped $YBa_2Cu_3O_{7-\delta}$ nanowires," *Supercond. Sci. Technol.*, vol. 33, no. 6, p. 064002, 2020.

[64] R. Arpaia, A. D'Alessio, E. Stepantsov, E. Wahlberg, E. Trabaldo, A. Kalaboukhov, T. Bauch, and F. Lombardi, "Engineering doping dependent CuO_2 nanoribbons in nm-thick a-axis $YBa_2Cu_3O_{7-\delta}$ films (submitted: June 2022),"

A | Appendix A

In this appendix all the information related to the nanofabrication process will be reported. The process has been already partly described in chapter 3.

1. A 30 nm thick YBCO film is deposited on a MgO substrate as described in chapter 2.
2. A 60 nm thick gold layer is evaporated on top of the film.
3. A 100 nm thick amorphous carbon film is deposited by PLD on top of the gold layer. The deposition is carried out at room temperature at an Ar background pressure of $3.4 \cdot 10^{-4}$. The laser energy is ramped up in three steps, from 70 (45 s), to 90 (45 s), to 110 mJ (2 min), to increase adhesion.
4. Before spinning the resist on top of the carbon mask, the surface is cleaned with IPA.
5. A double layer of e-beam resist is spin-coated on top of the C surface. The first (bottom) layer is MMC NANO Copolymer EL4 and the second (top), is ARP6200.13 Anisol 1:1. Both are spin coated at 6000 rpm for 60 s and baked at 95 degrees Celsius for 5 min.
6. The film is exposed by a 100 kV e-beam lithography system (JEOL JBX 9300 FS) in a pattern defined by a CAD mask. For small structures a current of 1 nA is employed, whereas for large ones the current of choice is 35 nA.
7. The resist is developed for 40 seconds in O-Oxylene 95% (top layer), followed by 35 seconds in MIBK:IPA 1:3 (bottom layer). The sample is then etched 5 s in 50 W oxygen RIE plasma to remove resist residues.
8. A 12 nm thick Cr metal mask is evaporated on the sample.
9. The Cr is lifted off by leaving it in a 60 degrees remover 1165 for 10 minutes.
10. The carbon not protected by Cr is etched for 25 minutes in a 50 W oxygen RIE plasma at 100 mbar oxygen pressure.

11. The YBCO that is not protected by the previously defined carbon mask is etched by Ar ion milling on a LN2 cooled stage. The voltage and current are set to the lowest setting that allows both stability of the ions stream and the etching of YBCO (300 V, 2 mA), to minimize the heating of the film. A neutralizer is used to minimize charging f the sample.

12. The remaining C on top of the nanostructures is etched by a low power (15 W) oxygen RIE plasma at 100 mbar oxygen pressure.

List of Figures

List of Tables

List of Symbols

Variable	Description	SI unit
T	temperature	K
$\boldsymbol{B}$	magnetic field	T
$\boldsymbol{E}$	electric field	V/m
$\boldsymbol{J}$	current density	A/m^2
R	resistance	Ohm (Ω)
p	pressure	bar

Acknowledgements

First of all I would like to thank my Politecnico supervisor, prof. Giacomo Ghiringhelli; even though we did not have the chance to properly know each other, I would still like to express my gratitude for the great chance I was given in doing my thesis here at Chalmers.

I would like to thank Floriana for taking me in her group, made of brilliant physicists and wonderful people, who made me feel welcome from the first day. Your creativity and passion for physics are two things that I won't easily forget.

I would like to thank Alex, for his help with the instruments I used.

I would like to thank Thilo, Xavier, Ananthu, and Kiryl; we did not work together but I am grateful for your help in the cleanroom in my first days at Chalmers and most importantly for all the nice moments we shared together.

My gratitude goes also to all the wonderful people I had the pleasure of sharing the D5 working area with; Thijs, my only one desk neighbour through all the way, thank you for your candid and unbounded dutchness, you were able to let me keep track of time just by the smell of your afternoon cup of noodles. Feike, we definitely shared many beautiful memories, but the things I will remember you for the most are your open-mindedness and your almost uncountable anecdotes; thank you, now I definitely know more about Frisian culture than I did before. Paul, thank you for having thought all of us how to master the art of chess playing, that is through constant practice with online chess games. Nuria, thank for having been one of the best desk-buddies one could ever want, thank you for your kindness and generosity throughout the way. Awse, I sat few meters above you, but we still had the chance of spend beautiful moments together; thank you for one of the best and richest meal of the last years. Andrea Napolitano, thank you for being one of the most proactive of us in the first months, without you I would still have no idea on how to play curling. I think that after all the nice time spent together I can call you friends and I really hope that our paths will cross again in the future.

Thank you Alessia for sharing with me the last stop of our university journey; thank you for the almost daily discussions we had together with Marco, which broke the monotony

of our lunch breaks. Thank you for being how you were, always kind and respectful, always needing to be pushed to hang out together but in the end always being someone to spend good time with.

Thank you Marco, for having been my friend throughout this journey, from the very beginning, when we took off in Italy without no idea of what we were getting into, till the very end, when it was definitely hard to say goodbye. We shared everything, from the first days in the temporary apartment we found, to the working area, to dinners with the friends we made along the way. We got two Notebooks in the end, but I think we would have been able to share one just as good. You maybe don't know, but your tips made me a better cook, and I hope that my unlimited passion for the country we did our thesis in, made you appreciate it a little bit more.

Thank you Edoardo, for being one of the kindest and nicest people I know. During the first times we did not really hang out together but the last weeks we made up for the time we lost. Going to the gym with you made my almost vain (thank you Brogyllen!) attempt to lose some weight much more fun. I found a friend in you, and I hope we will be able to meet in the future.

I would like to thank my parents, my mamma and my babbo, for having supported me in the last 25 years, but especially in the last months, when they allowed me the opportunity to do my thesis here at Chalmers, a little bit further than they would have wanted, but aware of how much this meant to me.

Finally, I would like to thank my Chalmers supervisor, Riccardo. Working with you has been the thing I liked the most about MC2, beating by far the Friday fikas, the ping pong table on the third floor and everything else. You were a great supervisor, but also a good friend; every day you made going to the workplace easier and you never complained, not even once, when held hostage in your own office and forced to chat with us master students for hours. You made some order in my chaotic approach to science, you taught me a lot of things and always pushed me to make that extra-step that always makes the difference. You are an endless source of information and at the same time an insightful scientist, which made the discussions I had with you very stimulating. I will always be grateful for the time you dedicated on me and for the time spent working with you, and I am sure I will benefit from it wherever I will work.